Large-eddy simulation of the flow and acoustic fields of a Reynolds number 10^5 subsonic jet with tripped exit boundary layers

Christophe Bogey,[a] Olivier Marsden,[b] and Christophe Bailly[c]
Laboratoire de Mécanique des Fluides et d'Acoustique, UMR CNRS 5509, Ecole Centrale de Lyon, Université de Lyon, 69134 Ecully Cedex, France

(Received 13 July 2010; accepted 22 January 2011; published online 11 March 2011)

Large-eddy simulations (LESs) of isothermal round jets at a Mach number of 0.9 and a diameter-based Reynolds number Re_D of 10^5 originating from a pipe are performed using low-dissipation schemes in combination with relaxation filtering. The aim is to carefully examine the capability of LES to compute the flow and acoustic fields of initially nominally turbulent jets. As in experiments on laboratory-scale jets, the boundary layers inside the pipe are tripped in order to obtain laminar mean exit velocity profiles with high perturbation levels. At the pipe outlet, their momentum thickness is $\delta_\theta(0)=0.018$ times the jet radius, yielding a Reynolds number $\mathrm{Re}_\theta=900$, and peak turbulence intensities are around 9% of the jet velocity. Two methods of boundary-layer tripping and five grids are considered. The results are found to vary negligibly with the tripping procedure but appreciably with the grid resolution. Based on analyses of the LES quality and on comparisons with measurements at high Reynolds numbers, fine discretizations appear necessary in the three coordinate directions over the entire jet flow. The final LES carried out using 252×10^6 points with minimum radial, azimuthal, and axial mesh spacings, respectively, of 0.20, 0.34, and $0.40\times\delta_\theta(0)$ is also shown to provide shear-layer solutions that are practically grid converged and, more generally, results that can be regarded as numerically accurate as well as physically relevant. They suggest that the mixing-layer development in the present tripped jet, while exhibiting a wide range of turbulent scales, is characterized by persistent coherent vortex pairings. © *2011 American Institute of Physics*. [doi:10.1063/1.3555634]

I. INTRODUCTION

The importance of initial conditions on free shear layers and jets is now well recognized. Following the pioneering works by Batt[1] and Hill *et al.*,[2] it has been shown by Gutmark and Ho[3] and Raman *et al.*,[4] for instance, that minute variations in the nozzle-exit conditions of initially laminar jets are able to cause significant changes in the downstream flow development. The effects of exit conditions have also been found to be spectacular on the transitional jets at moderate Reynolds numbers around 10^5 typically considered using laboratory facilities. Such transitional jets are indeed initially neither fully laminar nor fully turbulent. As discussed by Crighton,[5] Hussain[6] and Zaman,[7] among others, the turbulent and noise features of those jets therefore depend strongly on whether their nozzle-exit boundary layers contain low or high levels of velocity disturbances; i.e., whether they are nominally laminar (or weakly disturbed) or nominally turbulent (or highly disturbed).

The effects of the initial fluctuation levels on free shear flows have usually been investigated experimentally by installing devices inside the jet nozzle to trip the boundary layers, thus generating exit turbulent conditions for jets whose natural initial state would otherwise be laminar. This technique enables the exit turbulence levels to be varied for jets at fixed Reynolds numbers and is relatively easy to implement even if the trip parameters may need to be determined by trial and error until the outlet conditions are satisfactory. The trip devices themselves can be of various kinds. Rough strips,[2,7–11] rings,[4,12–18] or round wires[1,19,20] mounted at the nozzle inner wall, grids,[4] or screens[4,21,22] in the nozzle flow or pipe extensions[13,14,23–25] have, for example, been successfully applied. In most cases they have moreover been used for jets at moderate diameter-based Reynolds numbers over the range $5\times10^4\leq\mathrm{Re}_D\leq5\times10^5$, characterized by initial shear layers of momentum thicknesses δ_θ yielding Reynolds numbers Re_θ between 200 and 4000. To mention, for instance, the jet conditions in two sets of experiments, the Reynolds numbers were $\mathrm{Re}_D=1.4\times10^5$ and $\mathrm{Re}_\theta=700$ in a tripped round jet of Bridges and Hussain,[11] and they were between $10^5\leq\mathrm{Re}_D\leq2.5\times10^5$ and between $900\leq\mathrm{Re}_\theta\leq2250$ in the nominally turbulent jets of Zaman.[7,10]

In numerical simulations of jets, similar issues related to the influence of initial turbulence levels on the physical relevance of results have to be carefully taken into account. Because of the restrictions in terms of computational resources and despite rapid progress in the field over the past decade,[26–28] this has led the community to deal usually with low-Reynolds-number jets[29,30] or with initially laminar jets at moderate Reynolds numbers forced by disturbances of low magnitude.[31–34] Some attempts were made by Bogey

[a]Author to whom correspondence should be addressed. Present address: Centre Acoustique, Ecole Centrale de Lyon, 36, Avenue Guy de Collongue, 69134 Ecully Cedex, France. FAX: 33 4 72 18 91 43. Electronic mail: christophe.bogey@ec-lyon.fr.
[b]Electronic mail: olivier.marsden@ec-lyon.fr.
[c]Electronic mail: christophe.bailly@ec-lyon.fr.

et al.[35] and by Uzun and Hussaini[36] to compute initially turbulent jets. However, the former simulation was unfortunately under-resolved, whereas the latter was performed on a grid discretizing finely the upstream boundary layers, but whose spatial extent was limited to 4.5 diameters downstream of the nozzle exit. Strong vortex-pairing noise was also observed rather unexpectedly in the jet at $\mathrm{Re}_D=10^5$ studied by Uzun and Hussaini.[36] It can be emphasized that the simulation of initially fully turbulent jets at Reynolds numbers $\mathrm{Re}_D \geq 10^5$ is still a real challenge. A very large number of grid points are indeed required both for the turbulent boundary layers inside the nozzle and for the jet flow field developing outside, which should at least include the first 15 diameters downstream of the exit section. To bypass this difficulty, following the same approach as in experiments, we decided to perform simulations of jets whose boundary layers are tripped inside the nozzle to create highly disturbed but not fully turbulent nozzle-exit conditions.

In the present work, initially nominally turbulent subsonic round jets at Mach number 0.9 and Reynolds number $\mathrm{Re}_D=10^5$ are therefore calculated by compressible Large-eddy simulations based on relaxation filtering (LESs-RF) using low-dissipation and low-dispersion schemes. Inside a pipe nozzle, the jet boundary layers are tripped by the addition of random velocity disturbances to specify in all cases the same exit conditions as those measured in the tripped jets of Zaman.[7,10] The trip parameters are consequently adjusted so that the mean-velocity profiles at the nozzle exit roughly correspond to a laminar Blasius profile of momentum thickness $\delta_\theta=0.018$ times the pipe radius and that the peak turbulence intensities are around 9% of the jet velocity. The main objective in this work is to investigate the feasibility of computing nominally turbulent jets and then to establish some requirements for obtaining trustworthy numerical solutions for these flows. With this aim in view, two different methods of boundary-layer tripping and five meshes containing from 50×10^6 to 252×10^6 points are used. The effects of the trip procedure and of the grid resolution on the shear-layer transition, on the jet development as well as on the far-field noise determined by the LES, will thus be described in detail. The trends will be discussed from comparisons with experimental data for jets that are initially turbulent or at high Reynolds numbers. An *a posteriori* assessment of the accuracy of the simulations will also be performed by evaluating the quality of discretization. The convergence of the results with respect to the grid resolution will finally be explored, in particular from solutions computed for a supplementary jet with the same exit conditions as the jet considered here, except for a doubled boundary-layer thickness, using the finest mesh designed. The objective here will be to demonstrate that the jet turbulence is well taken into account by this mesh. The results obtained could then serve as reference solutions in future works.

The paper is organized as follows. In Sec. II, the parameters of the simulations and of the extrapolation of the LES near field to the far field, including numerical algorithm, computational grids, and times, are documented. The initial conditions of the jets are also reported. The influence of the boundary-layer tripping procedure on flow conditions at the pipe exit, on the mixing-layer development, and on the jet aerodynamic and far acoustic fields is investigated in Sec. III. The effects of grid resolution are then presented in Sec. IV. Concluding remarks are provided in Sec. V. Finally, the paper contains Appendixes A–D, devoted, respectively, to the definition of the tripping procedures and to an estimation of their generated noise, to a study of the quality of the shear-layer discretization, and to a comparison of the transfer functions of the dissipation mechanisms in the LES at the highest grid resolution.

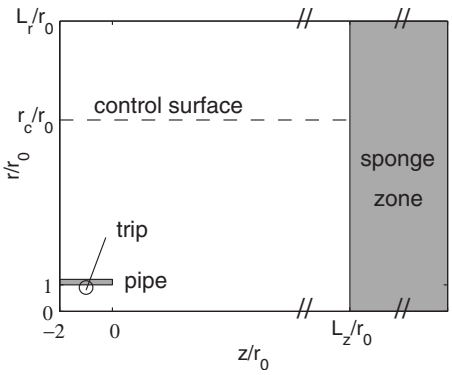

FIG. 1. Visualization in the (z,r) plane of the simulation configuration (the pipe thickness is here multiplied by 4). See Table I for the values of r_c, L_r, and L_z.

II. SIMULATION PARAMETERS

A. Jet definition

Six circular isothermal jets, hereafter referred to as Jetnoise256, Jetring256, Jetring256drdz, Jetring512, Jetring1024dz, and Jetring1024drdz depending on the boundary-layer tripping and grid used, are computed by Large-eddy simulation. They are all at Mach number $\mathrm{M}=u_j/c_a=0.9$ and at Reynolds number $\mathrm{Re}_D=u_jD/\nu=10^5$ and originate from a pipe nozzle of radius r_0 and length $2r_0$ as shown in Fig. 1 (u_j is the jet inflow velocity, c_a is the speed of sound in the ambient medium, $D=2r_0$ is the nozzle diameter, and ν is the kinematic molecular viscosity). The ambient temperature and pressure T_a and P_a are 293 K and 10^5 Pa. At the exit section of the nozzle at $z=0$, the width of the nozzle lip is $0.053r_0$. At the pipe inlet at $z=-2r_0$, laminar Blasius boundary layers of thickness $\delta=0.15r_0$ or equally of momentum thickness $\delta_\theta=0.018r_0$ yielding a Reynolds number $\mathrm{Re}_\theta=u_j\delta_\theta/\nu=900$ are imposed. The axial velocity profile is given by a polynomial approximation of the Blasius profile. In addition, radial and azimuthal velocities are initially set to zero, pressure is kept constant at its ambient value, and the temperature is determined by a Crocco–Busemann relation.

To specify nozzle-exit conditions as close as possible to those in the nominally turbulent jets of Zaman,[7,10] the boundary layers are tripped inside the pipe at $z\simeq-r_0$ as in Zaman's experiments. The tripping procedures are described in detail in Appendix A. They consist in simply adding in the boundary layer random velocity fluctuations of low amplitude to generate negligible spurious acoustic waves as indicated by

TABLE I. Simulation parameters: numbers of grid points n_r, n_θ, n_z, mesh spacings Δr at $r=r_0$, $r_0\Delta\theta$ and Δz at $z=0$, extents L_r, L_z of the physical domain, radial position r_c of the control surface, and time duration T.

	n_r, n_θ, n_z	$\Delta r/r_0$ (%)	$r_0\Delta\theta/r_0$ (%)	$\Delta z/r_0$ (%)	L_r, L_z	r_c/r_0	Tu_j/r_0
Jetnoise256	256, 256, 768	0.72	2.45	1.45	$11r_0, 32.5r_0$	7.25	475
Jetring256	256, 256, 768	0.72	2.45	1.45	$11r_0, 32.5r_0$	7.25	475
Jetring256drdz	290, 256, 992	0.36	2.45	0.72	$11r_0, 32.5r_0$	7.25	325
Jetring512	256, 512, 654	0.72	1.23	1.45	$11r_0, 25r_0$	7.25	475
Jetring1024dz	256, 1024, 962	0.72	0.61	0.72	$11r_0, 25r_0$	7.25	437.5
Jetring1024drdz	256, 1024, 962	0.36	0.61	0.72	$9r_0, 25r_0$	6.5	375
Jetring1024drdz2δ_θ	256, 1024, 687	0.36	0.61	0.72	$9r_0, 8r_0$	—	175

the calculations reported in Appendix B. These fluctuations are fully random both in time and in space in Jetnoise256, whereas they are based on vortical disturbances[31,35] decorrelated in the azimuthal direction in all other LESs. The tripping magnitudes are empirically chosen to obtain, at the nozzle exit of the six jets, turbulence intensities $u_e' \simeq 0.09u_j$ as well as mean-velocity profiles very similar to the laminar profiles of momentum thickness $\delta_\theta = 0.018r_0$ imposed at the pipe inlet, which will be illustrated in Sec. II C. It is indeed possible to find at the nozzle-exit section of tripped jets high levels of velocity fluctuations together with laminar velocity profiles, as clearly evidenced in the experimental works of Hussain and Zedan.[9]

To allow further examination of the grid convergence of the results, an additional jet, referred to as Jetring1024drdz2δ_θ, is simulated. In this case, a laminar boundary layer of thickness $\delta_\theta = 0.036r_0$, which is twice the thickness in the other jets, is imposed inside the pipe, and the *ring* tripping procedure is applied to obtain $u_e' \simeq 0.09u_j$ as previously. The jet Mach number remains M=0.9, but the diameter-based Reynolds number becomes $\mathrm{Re}_D = 5\times10^4$, in order not to change the Reynolds number $\mathrm{Re}_\theta = 900$. The initial shear-layer properties in Jetring1024drdz2δ_θ, namely, M, Re_θ, and u_e'/u_j, are therefore similar to those in the other jets.

B. LES procedures and parameters

The numerical methodology is identical to that used for recent simulations of initially laminar jets.[34] The LESs are carried out using a solver of the three-dimensional filtered compressible Navier–Stokes equations in cylindrical coordinates (r, θ, z) using low-dissipation and low-dispersion finite differences. The axis singularity is taken into account by the method proposed by Mohseni and Colonius.[37] Fourth-order 11-point centered finite differences are used for spatial discretization, and a second-order six-stage low-storage Runge–Kutta algorithm is implemented for time integration.[38] To circumvent the severe time-step restriction induced by the cylindrical coordinates, the derivatives in the azimuthal direction around the axis are calculated using every nth grid point, from $n=2$ up to $n=32$ or $n=64$ near the centerline, depending on the azimuthal resolution.[39] To remove grid-to-grid oscillations, a sixth-order 11-point centered filter designed to damp mainly the shortest waves discretized[40] is applied every time step to the flow variables. The discretization at the boundaries is performed by noncentered finite differences and filters with properties optimized in the Fourier space.[34,41] The filtering is also employed to dissipate subgrid-scale energy without significantly affecting the accurately resolved scales.[42] This LES approach was developed to avoid artificially decreasing the effective flow Reynolds number.[43] This point will be investigated in Appendixes C and D by evaluating the quality of discretization of the turbulent scales in the jets, as well as the transfer functions of the dissipation mechanisms in Jetring1024drdz. More details on the approach based on relaxation filtering, which can be referred to as LES-RF, are available in a specific paper.[44] Finally, in order to compute the radiated noise directly, nonreflective boundary conditions[45,46] are specified, with the addition of a sponge zone at the outflow. The nonreflective conditions are also applied at the pipe inlet to avoid acoustic resonance inside the nozzle as will be shown by velocity spectra in Secs. III A and IV A.

The computational setup is illustrated in Fig. 1. Some parameters of the LES grids used, containing from 50×10^6

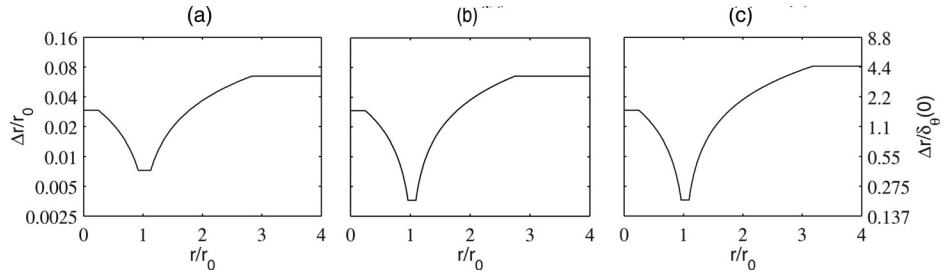

FIG. 2. Representation, in logarithmic scales, of the radial mesh spacing Δr normalized by the jet radius r_0 or by the exit boundary-layer thickness $\delta_\theta(0)$ in (a) Jetnoise256, Jetring256, Jetring512, and Jetring1024dz, (b) Jetring256drdz, and (c) Jetring1024drdz.

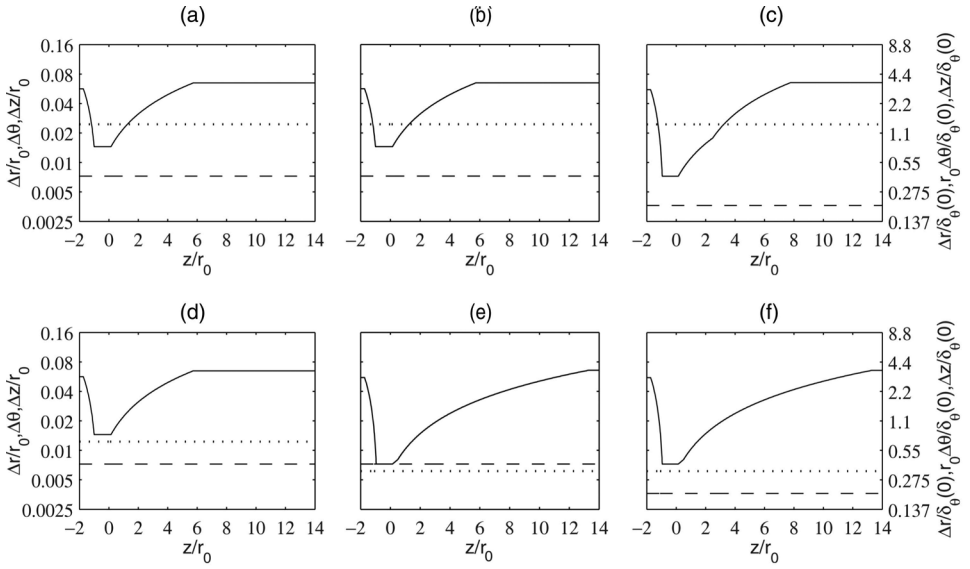

FIG. 3. Representation, in logarithmic scales, of the mesh spacings, —— Δz, – – – Δr, ····· $r_0\Delta\theta$, at $r=r_0$ in (a) Jetnoise256, (b) Jetring256, (c) Jetring256drdz, (d) Jetring512, (e) Jetring1024dz, and (f) Jetring1024drdz. The mesh spacings are normalized by r_0 or $\delta_\theta(0)$ as in Fig. 2.

up to 252×10^6 points, are provided in Table I. In Jetnoise256 and Jetring256, the azimuth is discretized by $n_\theta=256$ points, yielding $r_0\Delta\theta=0.0245r_0$, while the mesh spacings at the pipe lip are $\Delta r=0.0072r_0$ and $\Delta z=0.0145r_0$. In Jetring256drdz, $n_\theta=256$ is kept, but the mesh resolutions in the radial and the axial directions are twice as fine as previously at the nozzle lip. In Jetring512, $n_\theta=512$ points are specified in the azimuthal direction while using the radial and axial discretizations of Jetnoise256 and Jetring256. Two other configurations, Jetring1024dz and Jetring1024drdz, are studied using grids with $n_\theta=1024$ points in the azimuth, giving $r_0\Delta\theta=0.0061r_0$. Both grids are characterized by $\Delta z=0.0072r_0$ at $z=0$, but $\Delta r=0.0072r_0$ in Jetring1024dz, whereas $\Delta r=0.0036r_0$ in Jetring1024drdz at $r=r_0$. The physical domains, excluding the 80-point outflow sponge zones, extend axially up to $L_z=32.5r_0$ in the three LESs using $n_\theta=256$ but up to $L_z=25r_0$ in the LES using finer azimuthal resolutions. They extend radially up to $L_r=11r_0$ in the first five simulations but to $L_r=9r_0$ in Jetring1024drdz.

In the radial direction, the discretizations in the simulations Jetnoise256, Jetring256, Jetring512, and Jetring1024dz are the same. The radial mesh spacings Δr in these LESs are represented in Fig. 2(a) from $r=0$ to $r=4r_0$, normalized by the jet radius r_0 as well as by the exit boundary-layer thickness $\delta_\theta(0)$. The grids are stretched at rates lower than 4% to preserve numerical accuracy. This enables an excessive number of grid points to be avoided, and the inlet boundary layer to be discretized by 19 points using 62 points within the pipe radius. The maximum radial mesh spacing is obtained outside the jet flow for $r\geq3r_0$ and is equal to $\Delta r=0.065r_0$. The time frequency f of acoustic waves discretized by four grid points in this case corresponds to the Strouhal number $\mathrm{St}_D=fD/u_j=8.6$. The radial mesh spacings in Jetring256drdz and Jetring1024drdz are shown in Figs. 2(b) and 2(c). For $r\leq r_0$, they are identical and vary similarly to the mesh spacings in the other simulations. The resolution around $r=r_0$ is, however, twice as fine, and there are now 31 grid points in the boundary layer and 77 points within the pipe radius. For $r\geq r_0$, the grid stretching is applied to slightly more points in Jetring1024drdz, leading to $\Delta r=0.065r_0$ in Jetring256drdz but $\Delta r=0.081r_0$ in Jetring1024drdz for $r\geq3r_0$. Regarding the shear-layer discretization, it can be noted that the minimum mesh size, at $r=r_0$, is $\Delta r=0.40\delta_\theta(0)$ in Jetnoise256, Jetring256, Jetring512, and Jetring1024dz, but it is $\Delta r=0.20\delta_\theta(0)$ in Jetring256drdz and Jetring1024drdz. The radial mesh spacing is, however, smaller than $\delta_\theta(0)/2$ over $0.85r_0\leq z\leq1.15r_0$ in all LESs.

The variations in grid resolution along the lip line in the different simulations are displayed in Figs. 3(a)–3(f). The

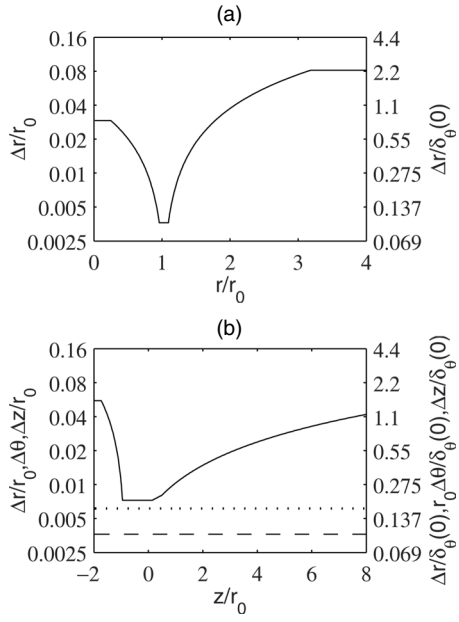

FIG. 4. Representation, in logarithmic scales, of the mesh spacings in Jetring1024drdz2δ_θ: (a) Δr as a function of r/r_0, (b) —— Δz, – – – Δr, and ····· $r_0\Delta\theta$ at $r=r_0$. The mesh spacings are normalized by r_0 or $\delta_\theta(0)$ as in Figs. 2 and 3.

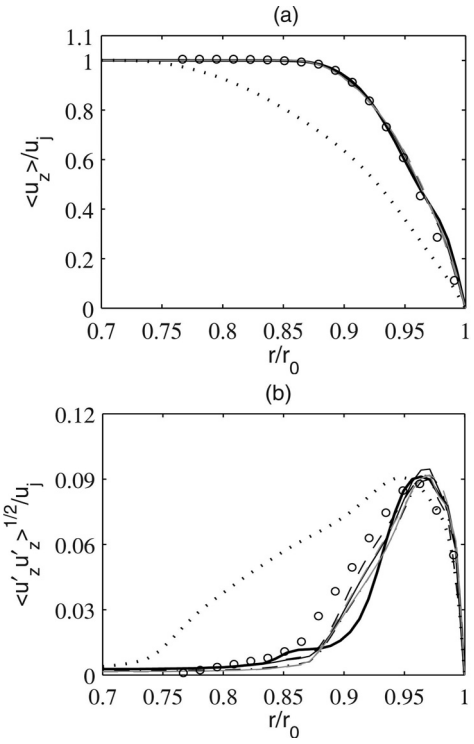

FIG. 5. Profiles at $z=0$ (a) of mean axial velocity $\langle u_z \rangle$ and (b) of the rms values of fluctuating axial velocity u_z' for —— (thick line) Jetnoise256, —— Jetring256, – – – Jetring256drdz, –·–·– Jetring512, gray solid line: Jetring1024dz, gray dashed line: Jetring1024drdz, and ····· Jetring1024drdz2δ_θ. Measurements for a Mach 0.18, tripped jet at $\mathrm{Re}_D=10^5$: ○ Zaman (Refs. 7 and 10).

radial and azimuthal mesh spacings are naturally constant and remain equal to their values at $z=0$ given in Table I. Concerning the discretization in the azimuthal direction, it can be remarked that $r_0\Delta\theta=1.36\delta_\theta(0)$ in the LES using $n_\theta=256$, which is rather coarse, whereas $r_0\Delta\theta=0.68\delta_\theta(0)$ using $n_\theta=512$ and $r_0\Delta\theta=0.34\delta_\theta(0)$ using $n_\theta=1024$. As for the discretization in the axial direction, the mesh spacings are minimum around the pipe exit and then increase in both the upstream and downstream directions. They remain, however, uniform in the pipe over $-r_0\leq z\leq 0$, which is between the trip location and the nozzle exit. Upstream of $z=-r_0$, the grids are stretched up to the inlet, so that there are 98 points in the pipe in Jetnoise256, Jetring256, and Jetring512 and 169 points in Jetring256drdz, Jetring1024dz, and Jetring1024drdz. Downstream of the nozzle, a grid stretching is also applied at rates lower than 1% to reach $\Delta z=0.065r_0$ at $z=5.7r_0$ in Jetnoise256, Jetring256, and Jetring512, at $z=7.8r_0$ in Jetring256drdz, and at $z=13.3r_0$ in Jetring1024dz and Jetring1024drdz. The axial grid resolution is, therefore, significantly higher in the final two LESs, around the nozzle lip, but also farther downstream nearly up to the end of the jet potential core. Compare, for instance, the mesh spacings Δz at $z=1.5r_0$ and $z=6r_0$: they are, respectively, equal to $1.5\delta_\theta(0)$ and $3.6\delta_\theta(0)$ in Jetring512 but to $0.7\delta_\theta(0)$ and $1.8\delta_\theta(0)$ in Jetring1024dz and Jetring1024drdz.

The numbers of time steps and the nondimensional times Tu_j/D of the jet simulations are provided in Table I. Between 81 000 and 164 000 iterations are done in the different LESs, corresponding to physical times between $325r_0/u_j$ to $475r_0/u_j$. To study jet features and to perform far-field extrapolation, density, velocity components, and pressure are recorded from time $t=125r_0/u_j$ at every point along $r=0$ and on the two surfaces at $r=r_0$ and $r=r_c=7.25r_0$ (note that $t=100r_0/u_j$ and $r_c=6.5r_0$ in Jetring1024drdz) at a sampling frequency allowing the computation of spectra up to a Strouhal number of 20. The velocity spectra are evaluated from overlapping samples of duration $27.4r_0/u_j$. The flow statistics are determined from $t=175r_0/u_j$, and they are averaged in the azimuthal direction.

Some parameters of the supplementary simulation Jetring1024drdz2δ_θ of a jet with a doubled initial shear-layer thickness are given in Table I. The grid used is that of Jetring1024drdz limited axially to $z=8r_0$, resulting in the mesh-spacing variations represented in Figs. 4(a) and 4(b). Compared to Jetring1024drdz, the computation of the mixing layer is performed in this case at twice the resolution. Due to the shear-layer thickening, one indeed gets, at the nozzle lip, $(\Delta r, r_0\Delta\theta, \Delta z)=(0.20, 0.34, 0.40)\times\delta_\theta(0)$ in Jetring1024drdz, but $(\Delta r, r_0\Delta\theta, \Delta z)=(0.10, 0.17, 0.20)\times\delta_\theta(0)$ in Jetring1024drdz2δ_θ.

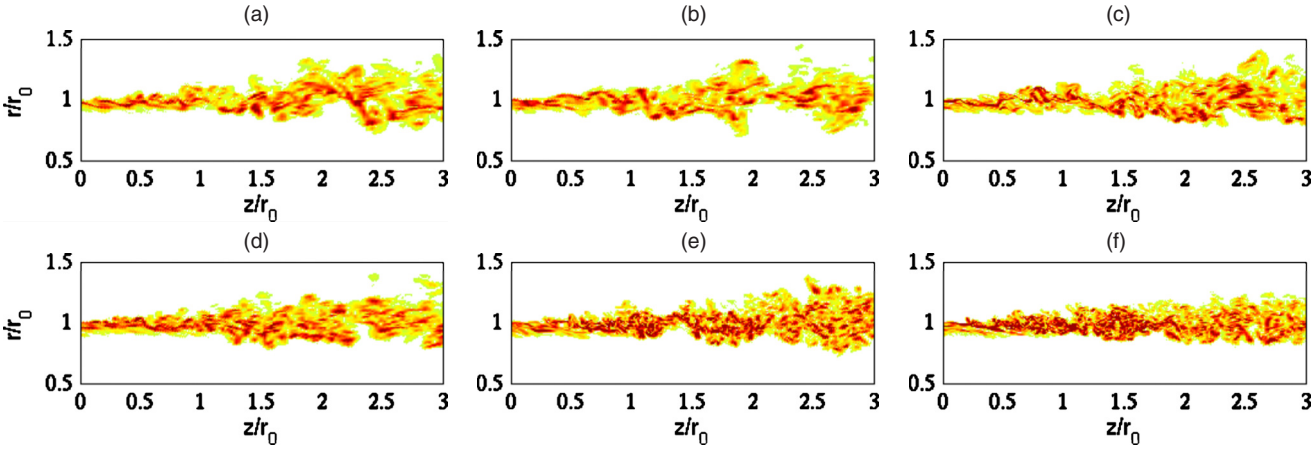

FIG. 6. (Color online) Snapshots in the (z,r) plane of vorticity norm just downstream of the pipe lip for (a) Jetnoise256, (b) Jetring256, (c) Jetring256drdz, (d) Jetring512, (e) Jetring1024dz, and (f) Jetring1024drdz. The color scale ranges up to the level of $25u_j/r_0$.

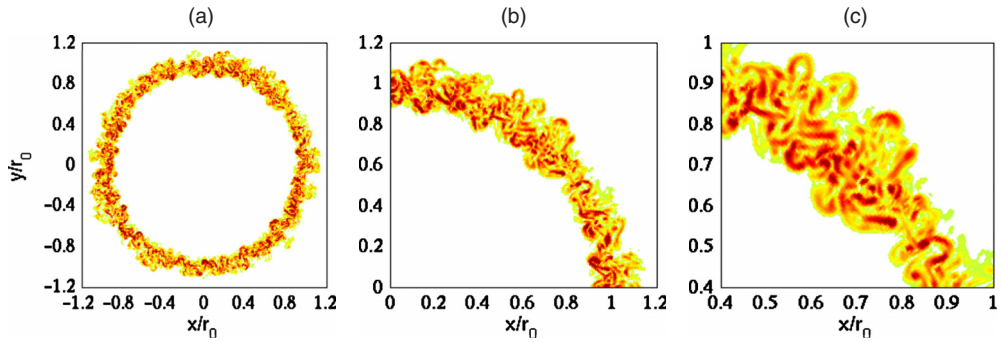

FIG. 7. (Color online) Snapshot in the (r,θ) or (x,y) plane at $z=r_0$ of vorticity norm for Jetring1024dz. Views over (a) $-1.2r_0 \leq x,y \leq 1.2r_0$, (b) $0 \leq x,y \leq 1.2r_0$, and (c) $0.4r_0 \leq x,y \leq r_0$. The color scale ranges up to the level of $34u_j/r_0$.

The LESs are carried out using NEC SX-8 computers. In particular, the simulation Jetring1024drdz is performed on seven processors using OpenMP, at a CPU speed around 36 Gflops, and requires around 7000 CPU h and 60 Gbytes of memory.

C. Nozzle-exit conditions

The profiles of mean and rms axial velocities obtained at the pipe exit for the different jets are presented in Figs. 5(a) and 5(b). The profiles of mean velocity $\langle u_z \rangle$ do not differ appreciably from the Blasius boundary-layer profiles imposed at the pipe inlet, leading to exit boundary-layer momentum thicknesses $\delta_\theta(0)=0.018r_0$ in the first six LESs and $\delta_\theta(0)=0.036r_0$ in Jetring1024drdz2δ_θ and to shape factors ranging from H=2.33 to H=2.40. The peak levels of velocity fluctuations are also all around 9% of the jet velocity. The present jets can therefore be considered as initially nominally turbulent. Focusing on the jets with $\delta_\theta(0)=0.018r_0$, they exhibit similar nozzle-exit conditions even if the rms profiles appear to vary slightly with the tripping method. Their initial conditions are, in addition, comparable to those measured by Zaman[7,10] in tripped jets, including a jet at $\mathrm{Re}_D=10^5$ as shown in Fig. 5. Finally, it is worth remembering that, in all cases, the Reynolds number based on $\delta_\theta(0)$ is $\mathrm{Re}_\theta=900$.

D. Vorticity and pressure snapshots

In order to illustrate the shear-layer development downstream of the nozzle lip in the six jets with $\delta_\theta(0)=0.018r_0$, snapshots of the vorticity norm obtained over $0 \leq z \leq 3r_0$ in the (z,r) plane are presented in Figs. 6(a)–6(f). As expected for initially turbulent jets, vortical structures are found immediately at the exit section. Both small and large structures are also observed in agreement with the Reynolds number $\mathrm{Re}_D=10^5$. A wider range of fine turbulent scales can, however, be noticed in the simulations using finer grids, especially in Jetring1024dz and Jetring1024drdz, whereas coherent structures may be more apparent in Jetnoise256 and Jetring256 using coarser grids.

Full and zoomed views of the vorticity field obtained at $z=r_0$ in Jetring1024dz are shown in Figs. 7(a)–7(c). They emphasize that mixing-layer turbulence is fully three-dimensional even rather close to the exit section. As will be discussed later from azimuthal velocity spectra, very small vortical structures can also be seen, especially in Fig. 7(c). They do not exhibit a clear preferred direction, and their typical sizes appear to be a few percent of the jet radius. An appropriate discretization of these scales should, therefore, require mesh spacings at most of $0.01r_0$. This constraint is,

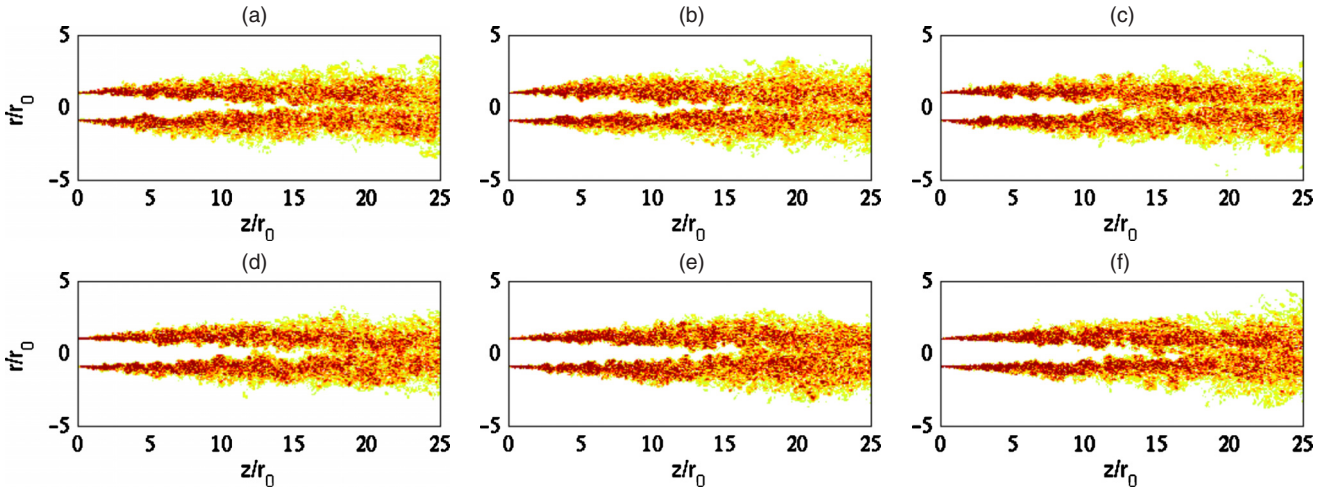

FIG. 8. (Color online) Snapshots in the (z,r) plane of vorticity norm up to $z=25r_0$ for (a) Jetnoise256, (b) Jetring256, (c) Jetring256drdz, (d) Jetring512, (e) Jetring1024dz, and (f) Jetring1024drdz. The color scale ranges up to the level of $5u_j/r_0$.

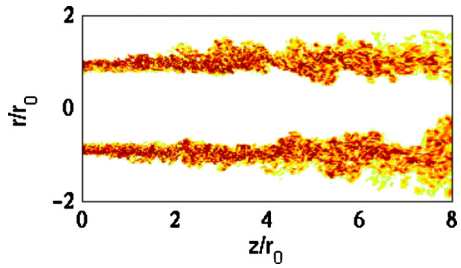

FIG. 9. (Color online) Snapshot in the (z,r) plane of vorticity norm for Jetring1024drdz2δ_θ. The color scale ranges up to the level of $20u_j/r_0$.

for instance, satisfied in the azimuthal direction with $n_\theta = 1024$ but is not with $n_\theta = 256$, refer to Table I.

To visualize the turbulent development of the jets, snapshots of vorticity fields obtained up to $z = 25r_0$ are represented in Figs. 8(a)–8(f). No appreciable difference in the jet flow fields can be distinguished. In particular, the end of the jet potential core appears to be located in all cases around 15 radii downstream of the nozzle exit.

A final snapshot of vorticity is provided in Fig. 9 for the jet with a doubled initial shear-layer thickness, simulated on the grid of Jetring1024drdz shortened in the axial direction to study grid convergence. As visible in the figure, only the shear-layer development is computed, up to $z = 8r_0$ or equally here to $z \simeq 225\delta_\theta(0)$. The mixing layer also shows a wide range of turbulent scales, as found previously for Jetring1024drdz in Fig. 6(f).

To give first insights into the noise radiated by the jets, snapshots of fluctuating pressure obtained directly by LES in the near field are presented in Figs. 10(a)–10(f). Even if isolated snapshots might be misleading and must consequently be interpreted with great caution, the pressure fields appear rather clean. Sound waves are visibly coming from the flow region located around $z = 2.5r_0$, where the shear-layer transition takes place. They may be of lower amplitude in the three bottom jets than in the three top jets computed using coarser azimuthal mesh grids. Compare, for instance, the pressure fields from Jetnoise256 in Fig. 10(a) and from Jetring1024drdz in Fig. 10(f). Remark also that no strong acoustic radiation can be clearly noticed from the pipe exit. This suggests that the noise generated by the boundary-layer tripping procedures is negligible, which will be verified in Appendix B.

E. Far-field extrapolation

The near fields obtained by LES are propagated to the far field using the wave-extrapolation method developed in recent work[34,47] by solving the linear acoustic equations in cylindrical coordinates. The numerical schemes and bound-

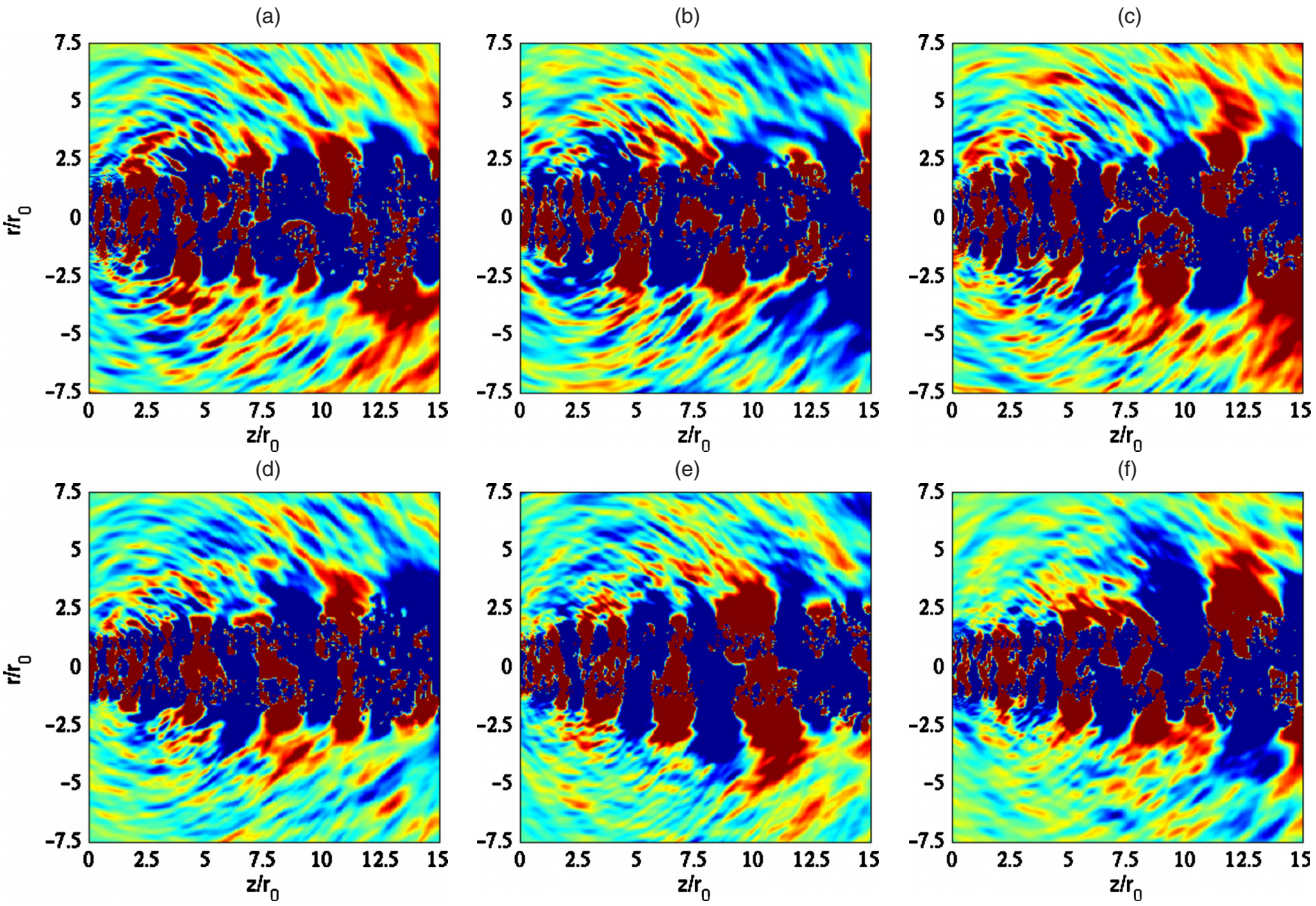

FIG. 10. (Color online) Snapshots in the (z,r) plane of fluctuating pressure $p - p_a$ obtained by LES for (a) Jetnoise256, (b) Jetring256, (c) Jetring256drdz, (d) Jetring512, (e) Jetring1024dz, and (f) Jetring1024drdz. The color scale ranges from levels of -100 to 100 Pa.

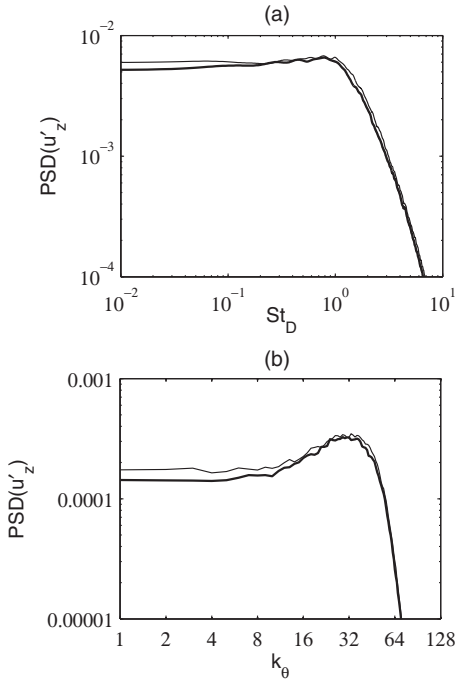

FIG. 11. Power spectral densities (PSDs) normalized by u_j of axial fluctuating velocity u_z' at $r=r_0$ and $z=0.4r_0$, as functions (a) of the Strouhal number $\mathrm{St}_D=fD/u_j$ and (b) of azimuthal wave number k_θ for —— (thick line) Jetnoise256 and —— Jetring256.

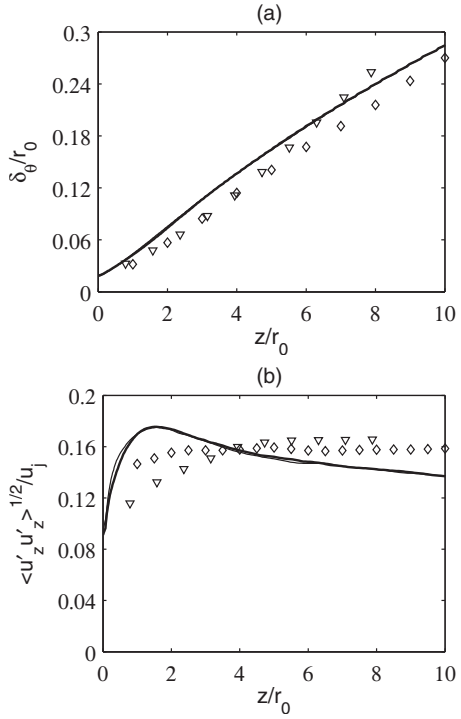

FIG. 12. Variations (a) of shear-layer momentum thickness δ_θ and (b) of the peak rms value of fluctuating velocity u_z' for —— (thick line) Jetnoise256 and —— Jetring256. Measurements: ▽ Husain and Hussain (Ref. 13) for an initially turbulent shear layer and ◇ Fleury *et al.* (Ref. 49) for a Mach 0.9 jet at $\mathrm{Re}_D=7.7\times10^5$.

ary conditions used are those of the LES. Noncentered finite differences and filters are applied at the inner-side boundary of the extrapolation grid. In practice, the extrapolation is performed from fluctuating velocities and pressure recorded in the LES from $t=125r_0/u_j$ at every point on the surface at $r=r_c=7.25r_0$ (in Jetring1024drdz $t=100r_0/u_j$ and $r_c=6.5r_0$) (see Fig. 1) at a frequency allowing the computation of spectra up to Strouhal number 20. These data are interpolated onto a cylindrical surface discretized by a uniform mesh spacing $\Delta z=0.065r_0$ in the axial direction. They are then imposed at the bottom boundary of a cylindrical grid of $n_r\times n_\theta\times n_z=835\times256\times1155$ points ($n_r=845$ in Jetring1024drdz), extending axially from $z=-16.6r_0$ to $z=58.2r_0$ and radially up to $r=61.4r_0$, on which the linear acoustic equations are solved. The grid mesh spacings are uniform with $\Delta r=\Delta z=0.065r_0$, yielding the Strouhal number $\mathrm{St}_D=8.6$ for four points per wavelength. After a propagation time of $t=60r_0/u_j$, pressure is recorded around the jets at a distance of $60r_0$ from $z=r=0$, where far-field acoustic conditions are expected to apply according to experiments,[48] during periods of $300r_0/u_j$ for Jetnoise256, Jetring256, and Jetring512, $140r_0/u_j$ for Jetring256drdz, $290r_0/u_j$ for Jetring1024dz, and $250r_0/u_j$ for Jetring1024drdz. Pressure spectra are then evaluated using overlapping samples of duration $38r_0/u_j$, and they are averaged in the azimuthal direction.

III. INFLUENCE OF THE TRIPPING PROCEDURE

In this section, the influence of the boundary-layer tripping method is investigated by comparing the main properties of the initial turbulence, of the shear-layer and jet flow developments and of the far-field noise obtained from Jetnoise256 and Jetring256 using the same grid but *noise* or *ring* tripping procedures inside the pipe.

A. Initial turbulence

As pointed out by Bridges and Hussain,[11] mean and rms velocity profiles may not be sufficient to characterize jet initial conditions, and velocity spectra should additionally be provided. Accordingly, spectra of axial velocity u_z' are computed in Jetnoise256 and Jetring256 just downstream of the nozzle lip at $r=r_0$ and $z=0.4r_0$. They are represented in Figs. 11(a) and 11(b), respectively, as functions of the Strouhal number $\mathrm{St}_D=fD/u_j$ and of azimuthal wave number k_θ. The velocity spectra from the two jets are remarkably similar, which suggests that the physical features of the jet initial turbulence do not depend much on the tripping method.

In Fig. 11(a), the frequency spectra from both simulations do not contain any distinct peak that might appear using an inappropriate trip device or a numerical setup generating forced turbulence. On the contrary, the spectra are all broadband and even rather flat for $\mathrm{St}_D\leq1$ as could be expected of white noise. This indicates that the jet initial conditions are satisfactorily clean.

Concerning the azimuthal spectra of velocity in Fig. 11(b), they are broadband, revealing significant components up to high wave numbers k_θ, which confirms that no mode strongly dominates at the jet exit. The spectra are flat for $k_\theta\leq16$, then reach maximum values for $k_\theta\simeq32$, and finally collapse sharply around $k_\theta=64$ as typically observed

TABLE II. Axial and azimuthal integral length scales $L_{uu}^{(z)}$ and $L_{uu}^{(\theta)}$ calculated from velocity u_z' at $r=r_0$ and $z=0.4r_0$.

	$L_{uu}^{(z)}/r_0$	$L_{uu}^{(\theta)}/r_0$
Jetring256	0.078	0.019
Jetring256drdz	0.076	0.022
Jetring512	0.067	0.016
Jetring1024dz	0.061	0.013
Jetring1024drdz	0.058	0.013

for a spectral truncation. The latter wave number indeed corresponds to the cutoff wave number of the relaxation filtering in the azimuthal direction, which is obtained for approximately four points per wavelength.

B. Shear-layer development

The variations over $0 \leq z \leq 10r_0$ of the shear-layer momentum thickness and of the maximum rms value of the fluctuating axial velocity in Jetnoise256 and Jetring256 are presented in Figs. 12(a) and 12(b). The profiles obtained from the two jets are seen to collapse, which supports that the tripping procedure has a negligible influence on the mean and turbulent developments of the mixing layers. In particular, the axial turbulence intensities in both jets reach notable peaks around $z=2r_0$, of magnitude $\langle u_z'^2\rangle^{1/2}=0.175u_j$ as reported in Table III.

For comparison, measurements obtained by Hussain and Zedan[9] for an initially turbulent axisymmetric mixing layer at a Mach number of 0.09 and a Reynolds number of 2.5×10^5 and by Fleury *et al.*[49] for a round jet at M=0.9 and $\mathrm{Re}_D=7.7\times10^5$ are also plotted in Figs. 12(a) and 12(b). While keeping in mind that comparisons between experimental and numerical data might be meaningless if the inflow conditions differ significantly, the shear layers appear to develop more rapidly, with higher rms fluctuating velocities, in the simulations. In Fig. 12(b) especially, the turbulence intensities in Jetnoise256 and Jetring256 show well-marked maxima shortly downstream of the nozzle exit, whereas they increase nearly monotonically in the experiments. The presence of such rms velocity peaks in the LES may be indicative of strong mixing-layer transitions. They might be caused by insufficient grid resolution, as will be examined in Sec. IV B.

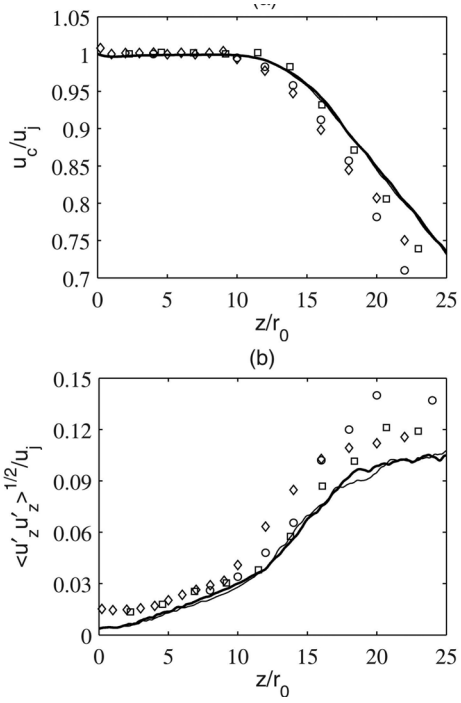

FIG. 13. Variations (a) of centerline mean axial velocity u_c and (b) of the rms value of fluctuating velocity u_z' at $r=0$ for —— (thick line) Jetnoise256 and —— Jetring256. Measurements for Mach 0.9 jets at $\mathrm{Re}_D \geq 5\times10^5$: ○ Lau *et al.* (Ref. 50), □ Arakeri *et al.* (Ref. 17), and ◇ Fleury *et al.* (Ref. 49).

C. Jet flow development

The variations along the centerline of the mean and rms values of axial velocity in Jetnoise256 and Jetring256 are presented in Figs. 13(a) and 13(b). In the same way as for the mixing-layer features in Figs. 12(a) and 12(b), the flow properties obtained at $r=0$ in the two simulations using different boundary-layer tripping methods are very similar. This demonstrates the weak influence of the trip device on the jet development. For further discussion, it can also be noted that in the jets the length of the potential core is $z_c=15.5r_0$, where z_c is here defined by $\langle u_z\rangle(z=z_c)=0.95u_j$, and that the rms value of axial velocity at the end of the potential core at $r=0$ and $z=z_c$ is equal to $\langle u_z'^2\rangle^{1/2}=0.072u_j$. These values can be found in Table IV.

Experimental data provided for jets at Mach number 0.9 by Lau *et al.*,[50] Arakeri *et al.*,[17] and Fleury *et al.*[49] are also represented in Figs. 13(a) and 13(b). The comparisons with the present simulation results can be regarded as meaningful because the above-mentioned jets are at Reynolds numbers

TABLE III. Peak rms values of axial and radial fluctuating velocities u_z' and u_r'.

	$\langle u_z'^2\rangle^{1/2}/u_j$	$\langle u_r'^2\rangle^{1/2}/u_j$
Jetring256	0.175	0.136
Jetring256drdz	0.177	0.135
Jetring512	0.158	0.125
Jetring1024dz	0.157	0.117
Jetring1024drdz	0.154	0.112

TABLE IV. Axial position of the end of the potential core z_c and rms values of axial and radial fluctuating velocities u_z' and u_r' at $r=0$ and $z=z_c$.

	z_c/r_0	$\langle u_z'^2\rangle^{1/2}/u_j$	$\langle u_r'^2\rangle^{1/2}/u_j$
Jetring256	15.4	0.072	0.056
Jetring256drdz	15.6	0.070	0.046
Jetring512	16.4	0.067	0.049
Jetring1024dz	15.2	0.082	0.069
Jetring1024drdz	15.9	0.075	0.069

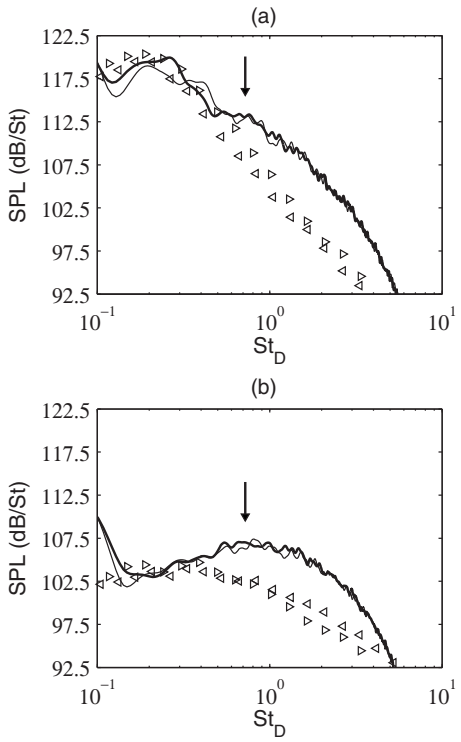

FIG. 14. Sound pressure levels (SPL) obtained at $60r_0$ from the jet exit as functions of $St_D=fD/u_j$ at the angles of (a) 30° and (b) 90° for —— (thick line) Jetnoise256 and —— Jetring256. The arrows indicate the frequency determined using $St_\theta=f\delta_\theta(0)/u_j=0.0065$. Measurements for jets at $Re_D \geq 7.8\times10^5$: ◁ Tanna (Ref. 51) and ▷ Bogey *et al.* (Ref. 52).

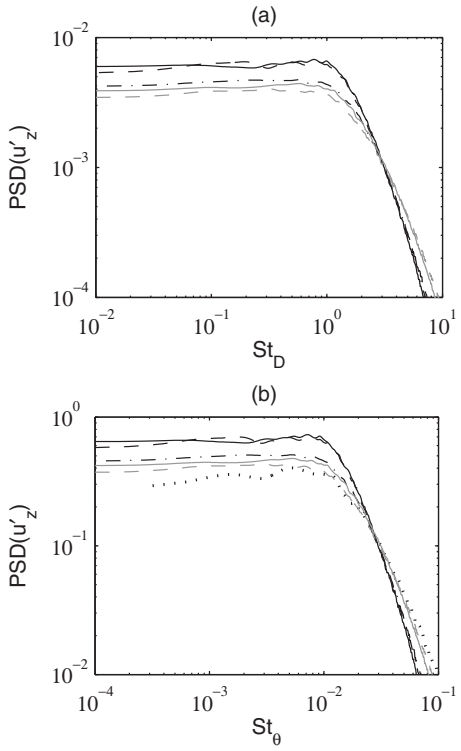

FIG. 15. PSDs normalized by u_j of axial fluctuating velocity u_z' at $r=r_0$ as functions (a) of $St_D=fD/u_j$ and (b) of $St_\theta=f\delta_\theta(0)/u_j$ for —— Jetring256, – – – Jetring256drdz, –·–·– Jetring512, gray solid line: Jetring1024dz, and gray dashed line: Jetring1024drdz at $z=0.4r_0$ and for ····· Jetring1024drdz2δ_θ at $z=0.8r_0$.

higher than 5×10^5. Therefore, these jets, albeit possibly initially laminar, all probably contain significant inflow turbulence. This is the case, for instance, in the jet of Arakeri *et al.*,[17] in which the peak rms values of u_z' at the exit section are around 10% of u_j. Compared to the experimental findings, the jets from Jetnoise256 and Jetring256 thus display potential cores of similar length, but farther downstream they are found to develop more slowly with lower turbulence intensities. These discrepancies will be shown to be reduced in Sec. IV C when finer grids are used.

D. Sound pressure fields

The pressure spectra estimated at $60r_0$ from the pipe exit at the radiation angles $\phi=30°$ and 90° relative to the jet direction are finally presented in Figs. 14(a) and 14(b). Based on the results shown in Appendix B, they are unlikely to be significantly contaminated by spurious waves generated by the tripping procedures. More importantly, the acoustic spectra from Jetnoise256 and Jetring256 are seen not to differ appreciably, as could be expected from the largely similar aerodynamic fields of the two jets.

For Strouhal numbers lower than 0.5, the sound spectra agree rather well with measurements[51,52] for jets at Reynolds numbers higher than 7.8×10^5, whereas additional humps are observed for the higher Strouhal numbers. These humps are broadband, and their peaks are located around a frequency corresponding to $St_\theta=f\delta_\theta(0)/u_j=0.0065$ when normalized by the initial shear-layer thickness. This Strouhal number is half of $St_\theta=0.013$, which, in turn, lies in the range of the most-amplified Strouhal numbers in axisymmetric mixing layers.[3] The humps in the sound spectra are, therefore, likely to result from a first stage of coherent vortex pairings in the shear layer, as found in initially laminar jets.[7,11,34] The presence of such noise sources in Jetnoise256 and Jetring256 is not so surprising given the vorticity and pressure snapshots of Figs. 6(a), 6(b), 10(a), and 10(b), as well as the strong mixing-layer transition observed in Fig. 12(b). At this point, it is difficult to state whether they are physically justified in the initially turbulent jet considered. This will be checked in Sec. IV from LES performed at higher grid resolution.

IV. EFFECTS OF THE GRID RESOLUTION

The impact of the grid resolution on the flow and acoustic fields of the tripped jet is now studied by comparing the results obtained from the simulations Jetring256, Jetring256drdz, Jetring512, Jetring1024dz, and Jetring1024drdz, using the same tripping method but different meshes. The convergence of the initial turbulence and shear-layer properties with respect to the grid is also examined from the solutions computed in Jetring1024drdz2δ_θ on the fine grid of Jetring1024drdz for the jet with thicker initial shear layer.

A. Initial turbulence

As previously in Sec. III A, spectra of fluctuating axial velocity are calculated just downstream of the pipe lip. The frequency spectra thus determined at $r=r_0$ and $z=0.4r_0$ for

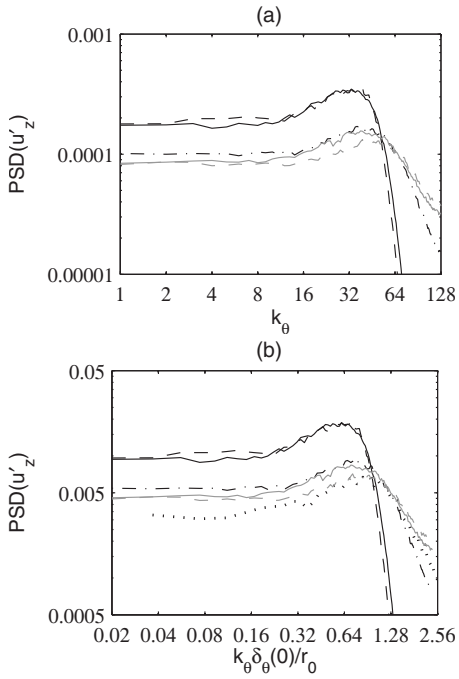

FIG. 16. PSDs normalized by u_j of fluctuating velocity u_z' at $r=r_0$ as functions (a) of wave number k_θ and (b) of $k_\theta\delta_\theta(0)/r_0$ for —— Jetring256, – – – Jetring256drdz, –·–·– Jetring512, gray solid line: Jetring1024dz, and gray dashed line: Jetring1024drdz at $z=0.4r_0$ and for ····· Jetring1024drdz2δ_θ at $z=0.8r_0$.

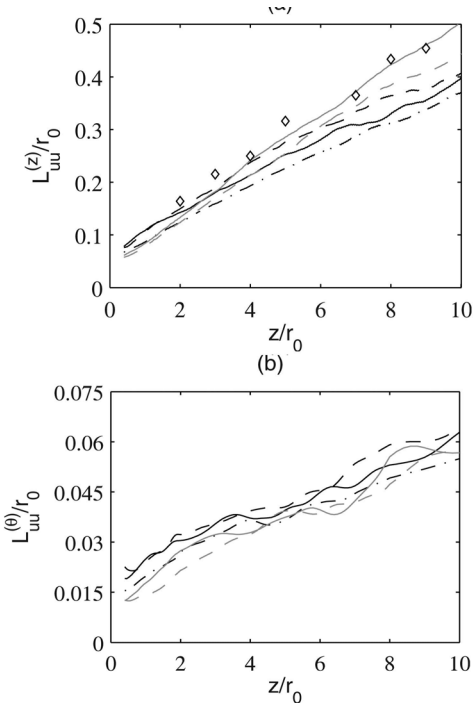

FIG. 17. Variations of the integral length scales (a) $L_{uu}^{(z)}$ and (b) $L_{uu}^{(\theta)}$, calculated from velocity u_z' at $r=r_0$ for —— Jetring256, – – – Jetring256drdz, –·–·– Jetring512, gray solid line: Jetring1024dz, and gray dashed line: Jetring1024drdz. Measurements: ◇ Fleury *et al.* (Ref. 49) for a Mach 0.9 jet at $\mathrm{Re}_D=7.7\times10^5$.

Jetring256, Jetring256drdz, Jetring512, Jetring1024dz, and Jetring1024drdz are represented in Fig. 15(a) as functions of the Strouhal number $\mathrm{St}_D=fD/u_j$. Despite slight changes in magnitude probably due to different flow developments between $z=0$ and $z=0.4r_0$, they display very similar shapes with flat regions for $\mathrm{St}_D\leq1$, indicating that the distribution of the frequency components of the jet initial disturbances does not vary much with the grid characteristics. The spectra from Jetring256 and Jetring256drdz, in particular, almost collapse, while those from Jetring512, Jetring1024dz, and Jetring1024drdz are relatively close. The latter spectra, when plotted as functions of $\mathrm{St}_\theta=f\delta_\theta(0)/u_j$ in Fig. 15(b), also agree reasonably well with the spectrum evaluated in Jetring1024drdz2δ_θ at $r=r_0$ and $z=0.8r_0$. This suggests a fair grid convergence of the pipe-exit turbulence properties in the LES using fine azimuthal discretizations.

The azimuthal spectra of velocity computed in the jets at the same positions as the frequency spectra are shown in Figs. 16(a) and 16(b). In Fig. 16(a), the spectra from Jetring256 and Jetring256drdz, using $n_\theta=256$, reach maximum values around $k_\theta=32$ and collapse rapidly for $k_\theta\geq64$. Those from Jetring512, Jetring1024dz, and Jetring1024drdz, using more n_θ points, while exhibiting roughly similar shapes, are smoother. The peak components, which are now at $k_\theta\simeq38$ in Jetring512 and Jetring1024dz and at $k_\theta\simeq44$ in Jetring1024drdz, are less pronounced, and the spectral decrease is less abrupt at high wave numbers. The turbulence energy is also distributed on higher modes between $k_\theta=64$ and $k_\theta=128$. The origin of the dominant wave numbers in the azimuthal spectra remains unclear, but they do not seem strongly related to the discretization. The spectra from Jetring1024drdz and Jetring1024drdz2δ_θ, when represented as functions of $k_\theta\delta_\theta(0)/r_0$ in Fig. 16(b), indeed appear nearly superimposed over the same range of wave numbers centered around $k_\theta\delta_\theta(0)/r_0\simeq0.8$, which supports that this initial flow feature is grid independent in Jetring1024drdz.

B. Shear-layer development

The sizes of the turbulence structures in the mixing layers are characterized by calculating the axial and azimuthal integral length scales $L_{uu}^{(z)}$ and $L_{uu}^{(\theta)}$ from velocity u_z' at $r=r_0$. Their values at $z=0.4r_0$, provided in Table II, are first found to depend mainly on the azimuthal resolution. Both $L_{uu}^{(z)}$ and $L_{uu}^{(\theta)}$ are, for example, reduced by roughly 25% when the number of points in the azimuth increases from 256 to 1024. It can also be worth noting that in all jets the initial azimuthal length scales are about four times smaller than the axial length scales, e.g., $L_{uu}^{(\theta)}=0.013r_0$ versus $L_{uu}^{(z)}=0.058r_0$ in Jetring1024drdz, which should be borne in mind when fixing grid parameters for jet simulations.

The variations of the integral scales $L_{uu}^{(z)}$ and $L_{uu}^{(\theta)}$ along the lip line up to $z=10r_0$, in other words upstream of the end of the jet potential core as will be shown later, are now presented in Figs. 17(a) and 17(b). As typically found experimentally, from the work by Davies *et al.*[53] to the Particle-Image-Velocimetry (PIV) measurements of Fleury *et al.*,[49] the length scales are observed to grow fairly linearly. More unexpectedly, they do not vary strongly with the grid. In Fig. 17(a), however, downstream of $z=4r_0$ the axial length scales are visibly larger in Jetring1024dz and Jetring1024drdz than in the other simulations, leading to a better fit with the ex-

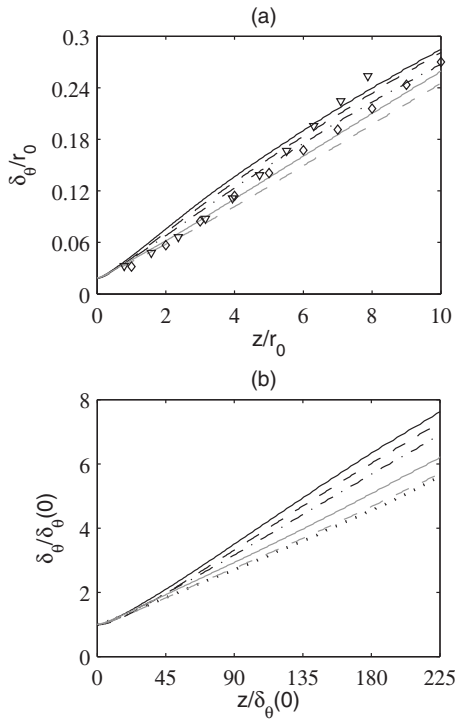

FIG. 18. Variations of shear-layer momentum thickness δ_θ normalized (a) by r_0 and (b) by $\delta_\theta(0)$ for —— Jetring256, – – – Jetring256drdz, –·–·– Jetring512, gray solid line: Jetring1024dz, gray dashed line: Jetring1024drdz, and ····· Jetring1024drdz2δ_θ. Measurements: ▽ Husain and Hussain (Ref. 13) for an initially turbulent axisymmetric shear layer and ◇ Fleury *et al.* (Ref. 49) for a Mach 0.9 jet at $\mathrm{Re}_D=7.7\times10^5$.

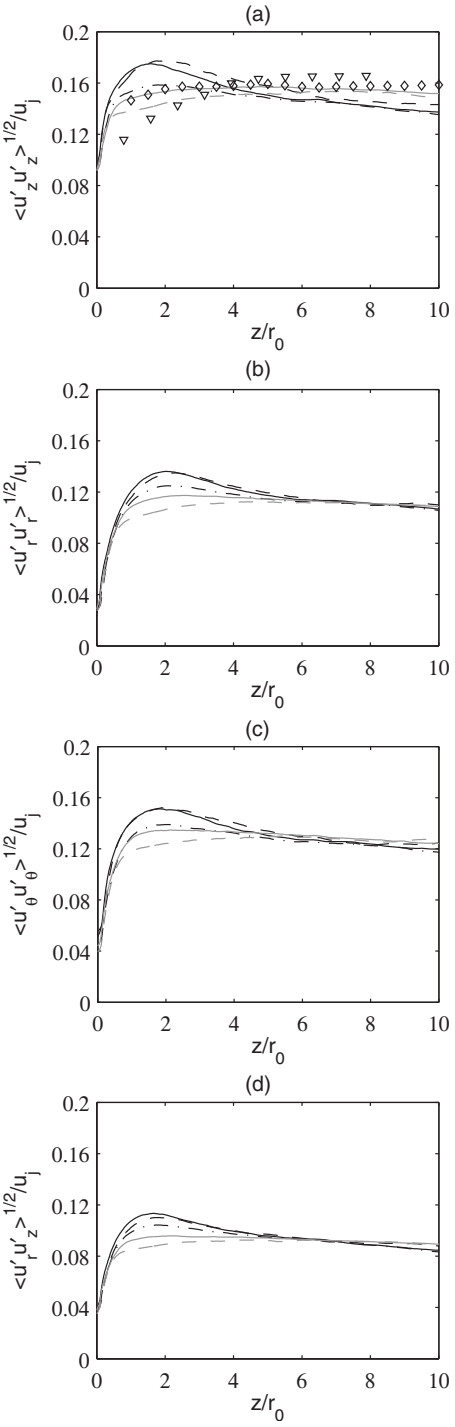

FIG. 19. Variations of the peak rms values of fluctuating velocities (a) u'_z, (b) u'_r, (c) u'_θ, and (d) of the peak magnitudes of Reynolds shear stress $\langle u'_r u'_z\rangle$ for —— Jetring256, – – – Jetring256drdz, –·–·– Jetring512, gray solid line: Jetring1024dz, and gray dashed line: Jetring1024drdz. Measurements: ▽ Husain and Hussain (Ref. 13) for an initially turbulent shear layer and ◇ Fleury *et al.* (Ref. 49) for a Mach 0.9 jet at $\mathrm{Re}_D=7.7\times10^5$.

perimental data obtained by Fleury *et al.*[49] for a jet at M $=0.9$ and $\mathrm{Re}_D=7.7\times10^5$. In Fig. 17(b), the azimuthal length scales also appear somewhat smaller in the LES using higher azimuthal resolution.

Based on the results above, the quality of shear-layer discretization in the LES is investigated in Appendix C by dividing the integral length scales by their corresponding local mesh sizes. The grids are found to provide suitable discretizations in both axial and azimuthal directions in Jetring1024dz and Jetring1024drdz but not in Jetring256, Jetring256drdz, and Jetring512. The radial grid resolution might, however, be low in Jetring1024dz, whereas it can reasonably be expected to be sufficient in Jetring1024drdz. The grid of Jetring1024drdz thus appears as the only grid likely to allow the computation of dependable mixing-layer solutions.

The physical relevance of the LES fields in Jetring1024drdz is furthermore supported by results given in Appendix D. From the transfer functions associated with molecular viscosity, relaxation filtering, and time integration, viscosity is indeed shown to be the dominant dissipation mechanism for the scales discretized at least by six or seven points per wavelength. The dynamics of the coherent structures developing in Jetring1024drdz, typically of the size of the axial integral length scales, should consequently not be significantly affected by undesirable dissipation.

Coming back to the LES output, the variations of the jet shear-layer momentum thickness are represented in Figs. 18(a) and 18(b), normalized by r_0 or by $\delta_\theta(0)$. They are plotted from $z=0$ up to $z=10r_0$ in Fig. 18(a), and up to $z=225\delta_\theta(0)$, namely, $z=4r_0$ with $\delta_\theta(0)=0.018r_0$ and $z=8r_0$ in Jetring1024drdz2δ_θ with $\delta_\theta(0)=0.036r_0$ in Fig. 18(b). In the former figure, the mixing layers are found to spread more slowly as the grid resolution gradually increases. In the early stage of shear-layer growth, up to $z\simeq4r_0$, the momentum-thickness profiles thus get closer to the measurements of

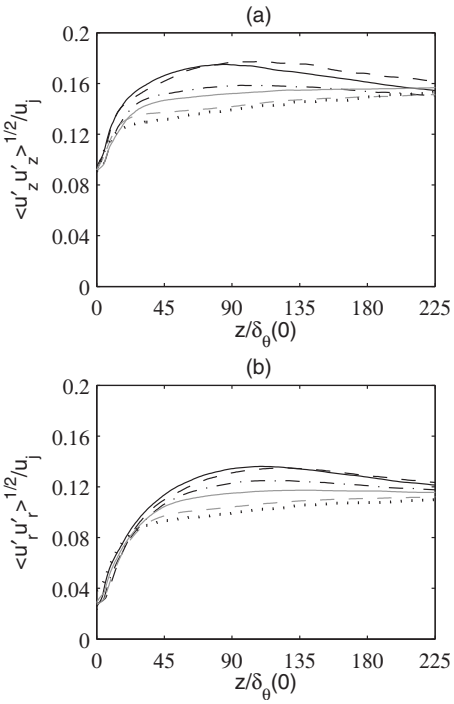

FIG. 20. Variations of the peak rms values of velocities (a) u_z' and (b) u_r' as functions of $z/\delta_\theta(0)$ for —— Jetring256, – – – Jetring256drdz, –·–·– Jetring512, gray solid line: Jetring1024dz, gray dashed line: Jetring1024drdz, and ····· Jetring1024drdz2δ_θ.

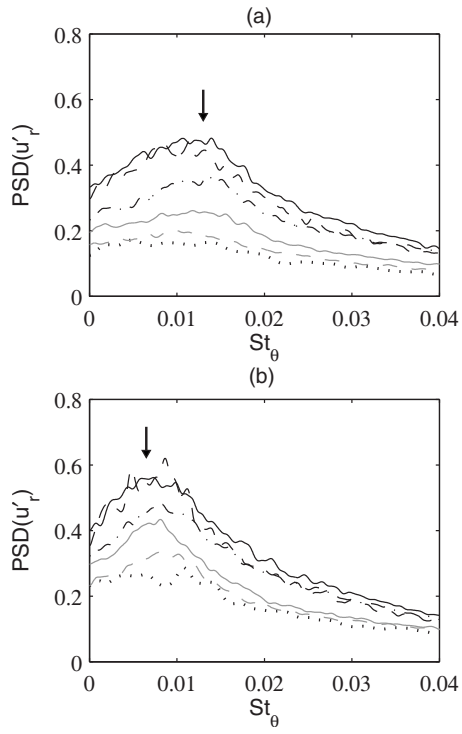

FIG. 21. PSDs normalized by u_j of radial velocity u_r' at $r=r_0$ as functions of $\mathrm{St}_\theta=f\delta_\theta(0)/u_j$ for —— Jetring256, – – – Jetring256drdz, –·–·– Jetring512, gray solid line: Jetring1024dz, and gray dashed line: Jetring1024drdz (a) at $z=1.5r_0$ and (b) at $z=3r_0$ and for ····· Jetring1024drdz2δ_θ (a) at $z=3r_0$ and (b) at $z=6r_0$. The arrows indicate (a) $\mathrm{St}_\theta=0.013$ and (b) $\mathrm{St}_\theta=0.0065$.

Hussain and Zedan[9] and of Fleury *et al.*[49] (see Sec. III B for the validity of the comparisons). In the latter figure, more spectacularly, the profiles obtained from Jetring1024drdz and Jetring1024drdz2δ_θ using the finest mesh grid can hardly be distinguished from each other. This demonstrates that grid convergence is achieved in Jetring1024drdz for the mean development of the jet mixing layers.

The variations over $0\leq z\leq 10r_0$ of the maximum rms values of velocities u_z', u_r', and u_θ' and of peak Reynolds shear stresses $\langle u_r'u_z'\rangle$ are shown in Figs. 19(a)–19(d). The profiles obtained from Jetring256 and Jetring256drdz using $n_\theta=256$ points do not differ much. They display remarkable peaks around $z=2r_0$, of magnitudes $\langle u_z'^2\rangle^{1/2}\simeq 0.175u_j$ and $\langle u_r'^2\rangle^{1/2}\simeq 0.136u_j$ as mentioned in Table III, which may be associated with strong shear-layer transitions. When more points are specified in the azimuth, the rms velocity profiles are considerably modified. Those determined from Jetring512 and Jetring1024dz using $n_\theta=512$ and $n_\theta=1024$ points exhibit smoother shapes and lower peak values, equal to $\langle u_z'^2\rangle^{1/2}=0.157u_j$ and $\langle u_r'^2\rangle^{1/2}=0.117u_j$ in Jetring1024dz, for example. In Jetring1024drdz, as the radial resolution at $r=r_0$ is doubled with respect to that in Jetring1024dz, the turbulence intensities still grow more gently with the axial position, with maximum values reduced to $\langle u_z'^2\rangle^{1/2}=0.154u_j$ and $\langle u_r'^2\rangle^{1/2}=0.112u_j$. They even increase nearly monotonically, in a similar way to that noticed for the experimental data in Fig. 19(a). It can finally be pointed out that for $z\geq 5r_0$ the turbulence intensities decrease in the first three LESs but remain high in the two others.

The discrepancies observed in Fig. 19 can be linked to the qualities of shear-layer discretization evaluated in Appendix C for the different LESs. Poor resolution in any grid direction just downstream of the jet exit appears to strengthen the mixing-layer transition, resulting in high peak values of turbulence intensities. An insufficient axial discretization along the lip line may also lead to low rms axial velocities downstream of $z=5$ or $6r_0$, as in Jetring512.

The profiles of the maximum rms values of u_z' and u_r' are now plotted for all jets in Figs. 20(a) and 20(b) as functions of $z/\delta_\theta(0)$ up to $z=225\delta_\theta(0)$. The results from Jetring1024drdz and Jetring1024drdz2δ_θ are very similar, which indicates that the turbulence intensities are practically grid converged in the shear layer of the former LES. The mixing-layer flow solutions from Jetring1024drdz can therefore be regarded as trustworthy, in agreement with the assessments of LES reliability reported in Appendixes C and D.

Spectra of velocity u_r' are finally computed along the lip line, at $z=1.5r_0$ slightly upstream of turbulence intensity peaks and at $z=3r_0$. They are represented, respectively, in Figs. 21(a) and 21(b) as functions of $\mathrm{St}_\theta=f\delta_\theta(0)/u_j$. They all display broadband shapes, especially with respect to spectra obtained in initially laminar jets[34] and maximum levels for similar Strouhal numbers. The highest components are more precisely found around $\mathrm{St}_\theta=0.013$ at $z=1.5r_0$ and $\mathrm{St}_\theta=0.0065$ at $z=3r_0$. The former frequency is typical of frequencies originally dominating in annular mixing layers,[3] which suggests the presence of a first stage of coherent vortex pairings. Their strengths are rather limited and decrease with higher grid resolution, but they seem persistent in the

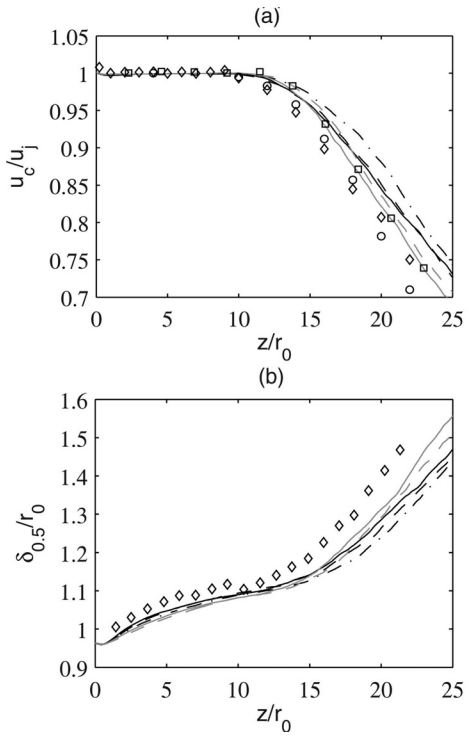

FIG. 22. Variations (a) of centerline mean axial velocity u_c and (b) of jet half-width $\delta_{0.5}$ for —— Jetring256, – – – Jetring256drdz, –·–·– Jetring512, gray solid line: Jetring1024dz, gray dashed line: Jetring1024drdz. Measurements for Mach 0.9 jets at $Re_D \geq 5\times10^5$: ○ Lau *et al.* (Ref. 50), □ Arakeri *et al.* (Ref. 17), and ◇ Fleury *et al.* (Ref. 49).

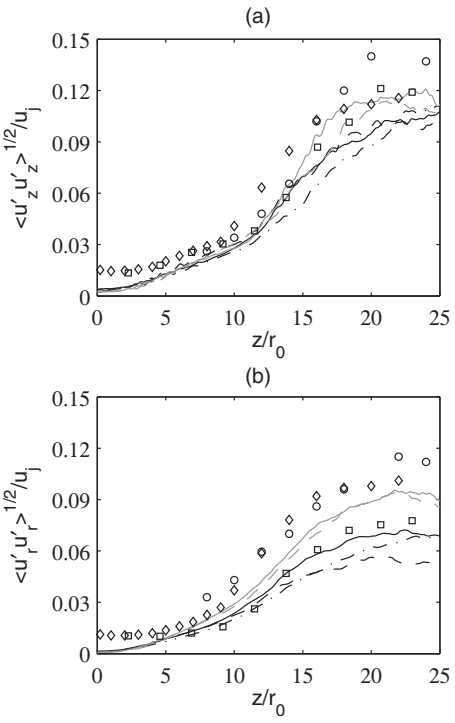

FIG. 23. Variations of centerline rms values of fluctuating velocities (a) u'_z and (b) u'_r for —— Jetring256, – – – Jetring256drdz, –·–·– Jetring512, gray solid line: Jetring1024dz, and gray dashed line: Jetring1024drdz. Measurements for Mach 0.9 jets at $Re_D \geq 5\times10^5$: □ Arakeri *et al.* (Ref. 17), ○ Lau *et al.* (Ref. 50), and ◇ Fleury *et al.* (Ref. 49).

jets regardless of the LES mesh. This claim is particularly supported by the fairly good comparison between the spectra from Jetring1024drdz and those calculated from Jetring1024drdz2 δ_θ at $z=3r_0$ and at $z=6r_0$ for a shear layer at the same Re_θ with a doubled initial thickness.

C. Jet flow development

The variations over $0\leq z\leq 25r_0$ of the centerline mean axial velocity and of the jet half width are presented in Figs. 22(a) and 22(b). As observed in the mixing layers in Fig. 18, the mean flows display very similar properties in the two jets computed using 256 points in the azimuthal direction despite different axial and radial discretizations. The potential core in this case ends around $z_c=15.5r_0$, where $\langle u_z\rangle \times(z=z_c)=0.95u_j$. In the other simulations, the potential core lengths vary only from $z_c=15.2r_0$ in Jetring1024dz to $z_c=16.4r_0$ in Jetring512, refer to Table IV, but the mean flow developments clearly change. The jets appear to spread farther downstream in Jetring512 but more rapidly in Jetring1024dz and Jetring1024drdz. With respect to the measurements plotted in the figure, provided for the Mach number 0.9 jets at $Re_D\geq 5\times10^5$, probably containing significant nozzle-exit turbulence as discussed in Sec. III C, the profiles from Jetring512 thus differ appreciably, whereas those from Jetring1024dz and Jetring1024drdz are much closer. For the centerline velocity decay, in Fig. 22(a), the agreement is even satisfactory.

The rms values of velocities u'_z and u'_r on the jet axis are shown in Fig. 23, together with experimental data from Lau *et al.*,[50] Arakeri *et al.*,[17] and Fleury *et al.*[49] as previously. They are lower in Jetring256drdz and Jetring512 than in Jetring256, but significantly higher in Jetring1024dz and Jetring1024drdz. For instance, at the end of the potential core at $r=0$ and $z=z_c$, the rms axial velocities range from $0.067u_j$ in Jetring512 to $0.082u_j$ in Jetring1024dz, and the rms radial velocities range from $0.046u_j$ in Jetring256drdz to $0.069u_j$ in Jetring1024dz and Jetring1024drdz (see all the values given in Table IV). The increase of the centerline turbulence levels with the grid resolution also results in levels corresponding fairly well to the measurements in Jetring1024dz and Jetring1024drdz, whereas they are underestimated in the other LES.

As could be expected, the best comparisons with experiments are consequently found for the jet flow fields from the two LES at highest resolutions. Remark, however, that using smaller mesh spacings in one direction while leaving coarse discretizations in the other directions, as done in Jetring512, may lead to poorer results.

D. Sound pressure fields

The overall sound pressure levels calculated at $60r_0$ from the pipe exit are presented in Fig. 24 for angles ϕ relative to the flow direction between 30° and 100°. They are very similar in Jetring256 and Jetring256drdz, which is not surprising given the nearly identical jet developments found in these LESs in Secs. IV B and IV C. In the same way, they do not differ much in Jetring512, Jetring1024dz, and Jetring1024drdz using higher azimuthal resolutions, except

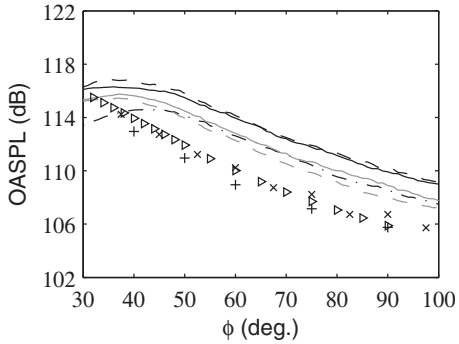

FIG. 24. Overall sound pressure levels at $60r_0$ from the pipe exit as functions of the angle ϕ relative to the jet direction for —— Jetring256, – – – Jetring256drdz, –·–·– Jetring512, gray solid line: Jetring1024dz, and gray dashed line: Jetring1024drdz. Measurements for jets at $\mathrm{Re}_D \geq 5\times10^5$: + Mollo-Christensen *et al.* (Ref. 54), × Lush (Ref. 55), and ▷ Bogey *et al.* (Ref. 52).

for $\phi<50°$. These simulations, moreover, provide weaker sound levels than the previous ones. Noise is lower by about 2 dB for $50° \leq \phi \leq 100°$, while it is decreased by 1.5 dB in Jetring1024dz and Jetring1024drdz and by 4 dB in Jetring512 at $\phi=30°$.

Compared to the measurements obtained by Mollo-Christensen *et al.*,[54] Lush,[55] and Bogey *et al.*[52] for jets at $M=0.9$ and $\mathrm{Re}_D \geq 5\times10^5$, the sound levels in the present jets at $\mathrm{Re}_D=10^5$ are larger for most emission angles. For $\phi \geq 50°$ in particular, they are higher by 4 dB in Jetring256 and Jetring256drdz and by 2 dB in Jetring512, Jetring1024dz, and Jetring1024drdz. For $\phi \simeq 30°$, numerical and experimental data, however, correspond reasonably well, apart from Jetring512 yielding significantly lower acoustic levels.

The pressure spectra estimated at $60r_0$ from the nozzle exit at the angles $\phi=30°$, 40°, 60°, and 90° are represented in Fig. 25 and compared with experimental data obtained for jets at the Reynolds numbers higher than 7.8×10^5. Unsurprisingly, the spectra from Jetring256 and Jetring256drdz are almost the same. They agree rather well with the measurements for the Strouhal numbers $\mathrm{St}_D \leq 0.5$, whereas additional humps appear for $\mathrm{St}_D \geq 0.5$. The spectra from the three other LES using finer grids have similar shapes, all especially containing strong components around $\mathrm{St}_D=0.072$ or equally $\mathrm{St}_\theta=0.0065$ here. As discussed in Sec. III D, this St_θ value suggests that the humps in the sound spectra are associated with a first stage of vortex pairings in the mixing layers. This link is further supported by the fact that this frequency is also close to half of the peak frequencies in the velocity spectra calculated at $r=r_0$ and $z=1.5r_0$, shown in Fig. 21(a).

The additional humps in the sound spectra with respect to the measurements are seen to be attenuated in the three LESs using finer meshes in which, interestingly, the jet shear-layer transitions are also characterized by lower turbulence intensities and smoother velocity spectra according to Figs. 19 and 21. The humps are, however, persistent and, since they do not appreciably differ in Jetring512 and in Jetring1024drdz using twice-as-fine discretizations in every grid direction, they are unlikely to be significantly affected by an extra increase of the grid resolution.

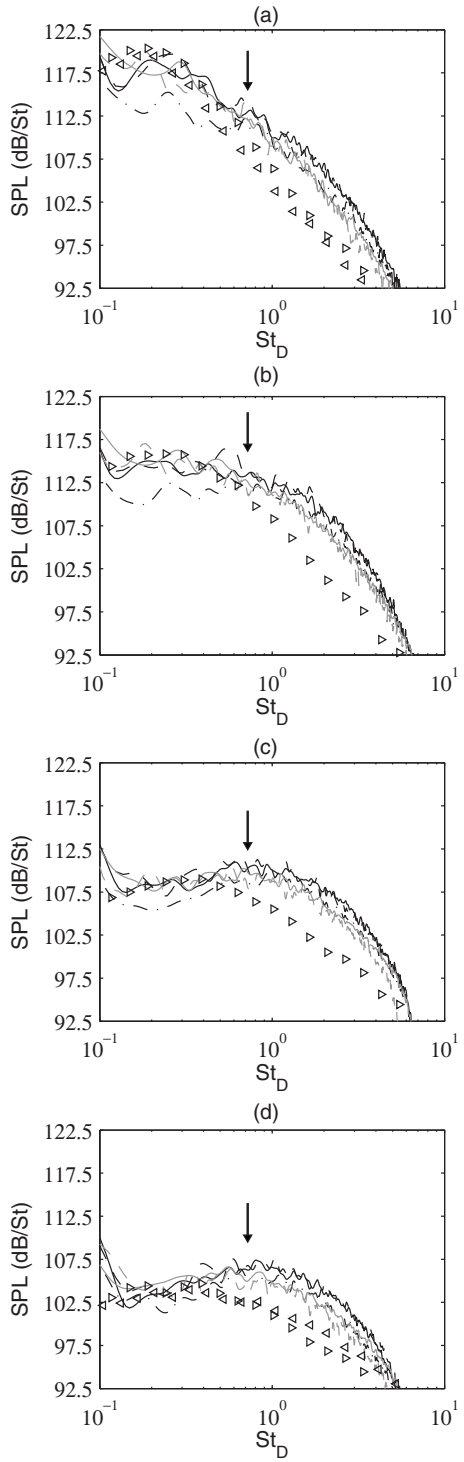

FIG. 25. SPLs at $60r_0$ from the jet exit as functions of $\mathrm{St}_D=fD/u_j$ at the angles of (a) 30°, (b) 40°, (c) 60°, and (d) 90° for —— Jetring256, – – – Jetring256drdz, –·–·– Jetring512, gray solid line: Jetring1024dz, and gray dashed line: Jetring1024drdz. The arrows indicate the frequency determined using $\mathrm{St}_\theta=f\delta_\theta(0)/u_j=0.0065$. Measurements for jets at $\mathrm{Re}_D \geq 7.8\times10^5$: ◁ Tanna (Ref. 51) and ▷ Bogey *et al.* (Ref. 52).

It can, moreover, be noted that the noise levels in Jetring512 are underestimated for $\mathrm{St}_D \leq 0.6$. This discrepancy can be related to the coarse axial discretization in this LES leading to low centerline turbulence intensities around the end of the potential core, refer to Fig. 23 and Table IV. The source generating the low-frequency noise component

dominating in the jet direction, which is probably located in this flow region,[56–59] may thus be weakened. The use of a finer axial discretization in Jetring1024dz and Jetring1024drdz fortunately removes this artifact, as indicated by the good agreement with measurements in this case.

The presence of noticeable vortex-pairing noise in the acoustic field of the present tripped jet may result from a combination of physical reasons. They will be investigated in future works, but some hypotheses are listed below. First, the jet, albeit tripped so as to exhibit peak turbulence intensities of 9% at the nozzle exit, is initially transitional but not fully turbulent.[7] Second, the flow Reynolds numbers $\mathrm{Re}_D=10^5$ and $\mathrm{Re}_\theta=900$ are moderate. The diameter-based Reynolds number is, in particular, not higher than the barrier value of $\mathrm{Re}_D=10^5$ which distinguishes low and high Reynolds number jet features according to some authors.[5,6] Finally, the issue of the perseverance of coherent structures in turbulent mixing layers can be mentioned.[19]

V. CONCLUSION

In the present paper, results provided by six compressible LES of an initially nominally turbulent round jet at Mach number 0.9 and Reynolds number 10^5 whose boundary layers are tripped inside a pipe nozzle are presented. They are found to vary in a negligible way with the tripping methodology but significantly with the grid resolution. To obtain satisfactory jet features, it appears that the discretization should be very fine not only at the nozzle lip but also all along the shear-layer development in the three grid directions. This implies, in particular, to avoid coarse azimuthal discretization, as well as rapid grid stretching in the axial direction, so as to properly calculate turbulence structures up to the end of the jet potential core.

Concerning the tripped jet considered, the flow and acoustic fields obtained from Jetring1024drdz using 252×10^6 points, with minimum radial, azimuthal, and axial mesh spacings equal, respectively, to 0.20, 0.34, and 0.40 times the pipe-exit boundary-layer momentum thickness, can be regarded as numerically accurate as well as physically relevant. This is supported by a grid-convergence study involving the simulation of a jet with a thicker initial shear layer, and by *a posteriori* assessments of the LES quality showing that in Jetring1024drdz turbulence structures are well discretized all along the jet development and that the dynamics of large scales are governed by molecular viscosity rather than by numerical or modeling dissipation. The mean and turbulent flow fields from Jetring1024drdz are also in good agreement with experimental data for jets at high Reynolds numbers. This is especially the case for the potential core length and for the downstream velocity decay. In addition, the increase of the turbulence intensities along the shear layer is smooth, as expected in an initially turbulent jet. As for the radiated noise, a component typically associated with coherent vortex pairings in the mixing layers is observed, yielding a hump in the sound spectra around 2 dB above the asymptotically low levels reached in jets at very high Reynolds numbers. Further works will be carried out to describe turbulent mechanisms in tripped jets. The influence of the initial turbulence levels and of the Reynolds number would notably be interesting points to characterize.

ACKNOWLEDGMENTS

This work was granted access to the HPC resources of the Institut du Développement et des Ressources en Informatique Scientifique (IDRIS) under the Allocation No. 2010-020204 made by Grand Equipement National de Calcul Intensif (GENCI). The authors are especially grateful to Jean-Michel Dupays from IDRIS for his technical assistance. They would also like to thank Dr. Khairul Zaman for his remarks on the present works.

APPENDIX A: TRIPPING PROCEDURES

In this appendix, the two procedures used to trip the jet boundary layers inside the pipe are described. They are developed to provide nozzle-exit conditions as close as possible to those in the nominally turbulent jets of Zaman.[7,10] The tripping magnitudes are, in particular, chosen to obtain peak turbulence intensities around 9% of the jet velocity in all cases.

In the method referred to as *noise* tripping, applied to Jetnoise256, velocity fluctuations fully random both in time and in space are added in the boundary layer between $z=-1.1r_0$ and $z=-0.9r_0$ for $r_0-\delta<r<r_0$, where δ is the thickness of the Blasius laminar profile considered. In practice, the three velocity components are modified in the following way:

$$\begin{Bmatrix} u_r \\ u_\theta \\ u_z \end{Bmatrix} = \begin{Bmatrix} u_r \\ u_\theta \\ u_z \end{Bmatrix} + \alpha u_j \begin{Bmatrix} \epsilon_r(r,\theta,z,t) \\ 2\epsilon_\theta(r,\theta,z,t) \\ 3\epsilon_z(r,\theta,z,t) \end{Bmatrix},$$

where $\epsilon_r(r,\theta,z,t)$, $\epsilon_\theta(r,\theta,z,t)$, and $\epsilon_z(r,\theta,z,t)$ are random numbers between -1 and 1 updated every time step at every grid point and $\alpha=0.00625$ to specify peak rms axial velocities around $0.09u_j$ at the jet exit.

In the *ring* tripping method, implemented in all other simulations, the velocity fluctuations introduced in the pipe are still random in time, but they are now divergence-free to minimize spurious acoustic waves. More precisely, they are based on vortical disturbances[31,35] which are not correlated in the azimuthal direction. The axial and radial velocities thus become every time step,

$$\begin{Bmatrix} u_r \\ u_z \end{Bmatrix} = \begin{Bmatrix} u_r \\ u_z \end{Bmatrix} + \epsilon_a(\theta,t)\alpha u_j \begin{Bmatrix} u_r^{ring} \\ u_z^{ring} \end{Bmatrix},$$

where $\epsilon_a(\theta,t)$ is a random number between -1 and 1 updated every iteration in every azimuthal section and α is set to 0.0706 in Jetring256, 0.0555 in Jetring256drdz, 0.059 in Jetring512 and Jetring1024dz, 0.045 in Jetring1024drdz, and 0.0635 in Jetring1024drdz2δ_θ. The velocities u_r^{ring} and u_z^{ring} are those of a unit vortex ring. They are expressed as

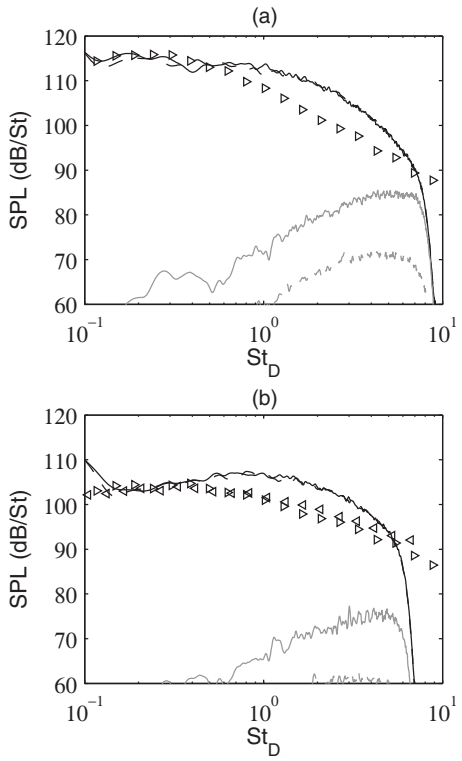

FIG. 26. SPLs at $60r_0$ from the jet exit as functions of $St_D=fD/u_j$ at the angles of (a) 40° and (b) 90° for Jetnoise256 with (black solid line) and without (gray solid line) jet flow and Jetring256 with (black dashed line) and without (gray dashed line) jet flow. Measurements for jets at $Re_D \geq 7.8 \times 10^5$: ◁ Tanna (Ref. 51) and ▷ Bogey *et al.*(Ref. 52).

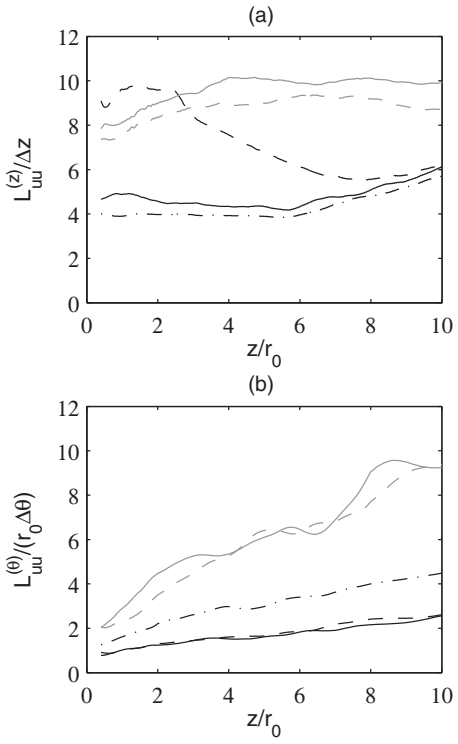

FIG. 27. Variations of the ratios (a) $L_{uu}^{(z)}/\Delta z$ and (b) $L_{uu}^{(\theta)}/(r_0\Delta\theta)$ between integral length scales calculated from u_z' and mesh spacings at $r=r_0$ for —— Jetring256, – – – Jetring256drdz, –·–·– Jetring512, gray solid line: Jetring1024dz, and gray dashed line: Jetring1024drdz.

$$\begin{Bmatrix} u_r^{ring} \\ u_z^{ring} \end{Bmatrix} = \frac{2r_{ring}}{rb}\exp\left(-\ln(2)\frac{a^2}{b^2}\right)\begin{Bmatrix} r-r_{ring} \\ z_{ring}-z \end{Bmatrix}$$

in which $a^2=(z-z_{ring})^2+(r-r_{ring})^2$ and b is equal to $2\Delta r$ in Jetring256, Jetring512, and Jetring1024dz, $4\Delta r$ in Jetring256drdz and Jetring1024drdz, and $8\Delta r$ in Jetring1024drdz2δ_θ. The vortex ring core is located at $z_{ring}=-0.95r_0$ and at $r_{ring}=r_0-\delta/2+\epsilon_r(\theta,t)\times\delta/6$, where $\epsilon_r(\theta,t)\in[-1,1]$ is a random number updated every time step in every azimuthal plane.

APPENDIX B: NOISE GENERATED BY THE TRIPPING

To characterize the noise from the tripping procedures, two additional simulations are performed using exactly the same parameters as in Jetnoise256 and Jetring256 but without jet flow. The acoustic waves generated are then propagated at $60r_0$ from the pipe exit using the wave-extrapolation method described in Sec. II E. The pressure spectra calculated in this way at the angles of 40° and 90° are represented in Fig. 26. At both angles, the noise radiated by the tripping procedures is significantly weaker than the noise emitted by Jetnoise256 and Jetring256. At 90°, in particular, the sound levels are lower by at least 20 dB using the noise tripping and by more than 30 dB using the ring tripping over the entire range of the Strouhal numbers of interest. The latter tripping method is thus quieter than the former while providing very similar results as shown in Sec. III. This is one of the reasons why it has been chosen to study the effects of grid resolution. It can also be pointed out that the tripping noise spectra contain no discernible tone, which indicates that there is no resonance inside the pipe nozzle.

APPENDIX C: QUALITY OF SHEAR-LAYER DISCRETIZATION

To discuss the quality of discretization of the shear-layer turbulence structures, the axial and azimuthal integral length scales determined at $r=r_0$ in Sec. IV B are divided by their corresponding local mesh spacings. The variations of $L_{uu}^{(z)}/\Delta z$ and $L_{uu}^{(\theta)}/(r_0\Delta\theta)$ thus obtained are represented in Figs. 27(a) and 27(b) up to $z=10r_0$. In Fig. 27(a), the axial length scales in Jetring256 and Jetring512 first appear to be discretized by fewer than five points upstream of $z=7r_0$, then by more points downstream because of the growth of turbulence scales in the axial direction. In Jetring512, in particular, $L_{uu}^{(z)}$ remains strikingly equal to $4\Delta z$ up to $z=6r_0$. Considering that the relaxation-filtering cutoff is at about four points per wavelength, the accuracy provided by the axial grid resolution in Jetring256 and Jetring512 might therefore be low. Fortunately, this should not be the case in the three other LES using finer axial discretizations. In Jetring256drdz one indeed obtains, for instance, $L_{uu}^{(z)}=9.1\Delta z$ initially at $z=0.4r_0$ and $L_{uu}^{(z)}=6.1\Delta z$ at $z=6r_0$, while in Jetring1024dz and Jetring1024drdz $L_{uu}^{(z)}>7.3\Delta z$ along the entire mixing layer, which is very satisfactory given the low-dispersion low-dissipation schemes used in the simulations.

In Fig. 27(b), the numbers of mesh points in the azimuthal integral length scales are also seen to vary signifi-

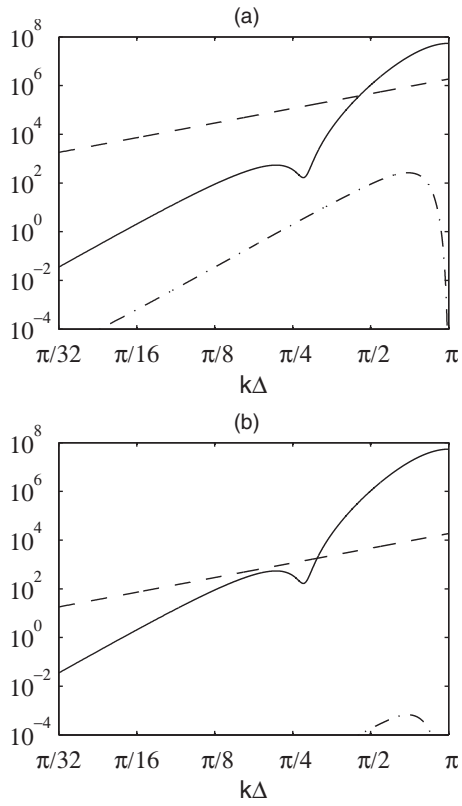

FIG. 28. Representation, in logarithmic scales, of the dissipation functions associated with —— relaxation filtering, – – – molecular viscosity, and –·–·– time integration in Jetring1024drdz, according to normalized wave number $k\Delta$ for (a) $\Delta=0.0036r_0$ and (b) $\Delta=0.036r_0$.

cantly. In Jetring256 and Jetring256drdz, $L_{uu}^{(\theta)}$ is, for example, smaller than $r_0\Delta\theta$ at $z=0.4r_0$, which can be related to the spectral-like truncation noticed in the azimuthal velocity spectra of Fig. 16. The length scales are, moreover, not discretized (i.e., $L_{uu}^{(\theta)}<2r_0\Delta\theta$) upstream of $z=7.5r_0$. This indicates clearly that the azimuthal grid resolution is insufficient when $n_\theta=256$. The integral scales $L_{uu}^{(\theta)}$ are, nevertheless, found to be much better taken into account when 512 or 1024 points are specified in the azimuthal direction. In Jetring512, they contain more than two grid points downstream of $z=1.7r_0$. In Jetring1024dz and Jetring1024drdz, more importantly, they are discretized immediately from the nozzle exit, with $L_{uu}^{(\theta)}=2r_0\Delta\theta$ at $z=0.4r_0$, and they are well calculated (i.e., $L_{uu}^{(\theta)}>4r_0\Delta\theta$) approximately downstream of $z=2r_0$.

The mesh grids of Jetring1024dz and Jetring1024drdz consequently appear to provide suitable discretizations of the shear layers both in the axial and azimuthal directions. The radial mesh spacings, however, differ in the two LESs, as reported in Table I and illustrated in Figs. 3(e) and 3(f), which may result in varying qualities of discretization in the radial direction. At $z=0$ and $r=r_0$, one indeed gets, for instance, $\Delta r=\Delta z$ in Jetring1024dz but $\Delta r=\Delta z/2$ in Jetring1024drdz. Rough estimations of the ratios between the radial integral length scales $L_{uu}^{(r)}$ and mesh sizes Δr can be obtained in these cases by assuming, according to the properties of homogeneous isotropic turbulence[60,61] as well as to measurements in jets,[49] that $L_{uu}^{(r)}\simeq L_{uu}^{(z)}/2$ in the jet mixing layers. The values of $L_{uu}^{(r)}/\Delta r$ just downstream of the pipe lip may thus be slightly lower than 4 in Jetring1024dz but around 8 in Jetring1024drdz. This suggests that the radial discretization of the shear-layer turbulence might be relatively coarse in Jetring1024dz but is likely to be appropriate in Jetring1024drdz.

APPENDIX D: DISSIPATION TRANSFER FUNCTIONS

The contributions of the three dissipation mechanisms in the present LESs, related, respectively, to molecular viscosity, relaxation filtering, and time integration, are finally examined in the simulation Jetring1024drdz at the highest grid resolution. This is done by determining their corresponding transfer functions according to the normalized wave number $k\Delta$, where Δ is an arbitrary mesh size.

The dissipation transfer function associated with molecular viscosity is given by νk^2 when classically represented according to dimensional wave number k, which directly yields $\nu(k\Delta)^2/\Delta^2$ according to $k\Delta$. Concerning the relaxation filtering, it is applied to the flow variables every time step Δt at a strength $\sigma=0.99$ using a sixth-order 11-point explicit filter.[40] Its transfer function according to $k\Delta$ is $\sigma D^*(k\Delta)/\Delta t$, where $D^*(k\Delta)$ is the damping factor of the filter, refer to previous papers.[42,44] The dissipation transfer function of time integration is finally derived from the amplification factor per time step $|G(\omega\Delta t)|$ of the Runge–Kutta scheme.[38] This factor depends on the normalized pulsation $\omega\Delta t=u_{conv}(k^*\Delta)\Delta t/\Delta$, where u_{conv} is taken as $2u_j/3$ and k^* is the approximated wave number estimated by the finite differences for wave number k. By analogy with the relaxation filtering, the transfer function associated with time integration is then $[1-|G(\omega\Delta t)|]/\Delta t$.

The above-defined functions are represented in Fig. 28 for the two mesh sizes $\Delta=0.0036r_0$ and $\Delta=0.036r_0$ in Jetring1024drdz. The first mesh size corresponds to the radial spacing Δr at $r=r_0$, see in Table I. The second one is approximately Δz at $z=6.7r_0$ as illustrated in Fig. 3(f). For both mesh sizes, the transfer function associated with time integration is first observed well below the two others for all wave numbers. The dissipation due to the numerical time integration is thus negligible compared to viscous and relaxation-filtering dissipation, which is rather expected given the very low damping factor of the six-stage Runge–Kutta algorithm.[38] For $\Delta=0.0036r_0$, in Fig. 28(a), the transfer function of molecular viscosity is found to be higher than that of the relaxation filtering for $k\Delta<1.4$ and inversely lower for $k\Delta>1.4$. This implies that most of the dissipation in this case results from molecular viscosity for the scales discretized by more than $\lambda/\Delta=4.4$ points per wavelength, whereas smaller scales are mainly damped by the relaxation filtering. A similar behavior is noticed in Fig. 28(b) for $\Delta=0.036r_0$. Here, the two dissipation functions intersect at $k\Delta=0.98$, which is for $\lambda/\Delta=6.4$ points per wavelength.

These results are important because they indicate that in Jetring1024drdz, thanks to the joint use of a highly selective filtering and of a very fine grid, the dynamics of the large turbulence structures can be expected to be mainly governed

by molecular viscosity and not by numerical or subgrid-modeling dissipation. The effective Reynolds number of the jet computed in this LES should, therefore, correspond to the Reynolds number of $Re_D=10^5$ specified by the flow initial conditions and not be artificially decreased.[43]

[1]R. G. Batt, "Some measurements on the effect of tripping the two-dimensional shear layer," AIAA J. **13**, 245 (1975).
[2]W. G. Hill, R. C. Jenkins, and B. L. Gilbert, "Effects of the initial boundary-layer state on turbulent jet mixing," AIAA J. **14**, 1513 (1976).
[3]E. Gutmark and C.-M. Ho, "Preferred modes and the spreading rates of jets," Phys. Fluids **26**, 2932 (1983).
[4]G. Raman, K. B. M. Q. Zaman, and E. J. Rice, "Initial turbulence effect on jet evolution with and without tonal excitation," Phys. Fluids A **1**, 1240 (1989).
[5]D. G. Crighton, "Acoustics as a branch of fluid mechanics," J. Fluid Mech. **106**, 261 (1981).
[6]A. K. M. F. Hussain, "Coherent structures—Reality and myth," Phys. Fluids **26**, 2816 (1983).
[7]K. B. M. Q. Zaman, "Far-field noise of a subsonic jet under controlled excitation," J. Fluid Mech. **152**, 83 (1985).
[8]A. K. M. F. Hussain and M. F. Zedan, "Effects of the initial condition on the axisymmetric free shear layer: Effects of the initial momentum thickness," Phys. Fluids **21**, 1100 (1978).
[9]A. K. M. F. Hussain and M. F. Zedan, "Effects of the initial condition on the axisymmetric free shear layer: Effects of the initial fluctuation level," Phys. Fluids **21**, 1475 (1978).
[10]K. B. M. Q. Zaman, "Effect of the initial condition on subsonic jet noise," AIAA J. **23**, 1370 (1985).
[11]J. E. Bridges and A. K. M. F. Hussain, "Roles of initial conditions and vortex pairing in jet noise," J. Sound Vib. **117**, 289 (1987).
[12]F.-R. Grosche, "Distributions of sound source intensities in subsonic and supersonic jets," *Proc. AGARD Conference on Noise Mechanisms*, Brussels, 1973, AGARD CP-131-4.
[13]Z. D. Husain and A. K. M. F. Hussain, "Axisymmetric mixing layer: Influence of the initial and boundary conditions," AIAA J. **17**, 48 (1979).
[14]A. K. M. F. Hussain and Z. D. Husain, "Turbulence structure in the axisymmetric free mixing layer," AIAA J. **18**, 1462 (1980).
[15]J. Lepicovsky and W. H. Brown, "Effects of nozzle exit boundary-layer conditions on excitability of heated free jets," AIAA J. **27**, 712 (1989).
[16]G. Raman, E. J. Rice, and E. Reshotko, "Mode spectra of natural disturbances in a circular jet and the effect of acoustic forcing," Exp. Fluids **17**, 415 (1994).
[17]V. H. Arakeri, A. Krothapalli, V. Siddavaram, M. B. Alkislar, and L. Lourenco, "On the use of microjets to suppress turbulence in a Mach 0.9 axisymmetric jet," J. Fluid Mech. **490**, 75 (2003).
[18]P. J. Morris and K. B. M. Q. Zaman, "Velocity measurements in jets with application to noise source modelling," J. Sound Vib. **329**, 394 (2010).
[19]I. Wygnanski, D. Oster, H. Fiedler, and B. Dziomba, "On the perseverance of a quasi-two-dimensional eddy-structure in a turbulent mixing layer," J. Fluid Mech. **93**, 325 (1979).
[20]J. H. Bell and R. D. Mehta, "Development of a two-stream mixing layer from tripped and untripped boundary layers," AIAA J. **28**, 2034 (1990).
[21]P. J. Strykowski and S. Russ, "The effect of boundary-layer turbulence on mixing in heated jets," Phys. Fluids A **4**, 865 (1992).
[22]S. Russ and P. J. Strykowski, "Turbulent structure and entrainment in heated jets: The effect of initial conditions," Phys. Fluids A **5**, 3216 (1993).
[23]L. Maestrello and E. McDaid, "Acoustic characteristics of a high-subsonic jet," AIAA J. **9**, 1058 (1971).
[24]R. A. Antonia and Q. Zhao, "Effect of initial conditions on a circular jet," Exp. Fluids **31**, 319 (2001).
[25]G. Xu and R. A. Antonia, "Effects of different initial conditions on a turbulent free jet," Exp. Fluids **33**, 677 (2002).
[26]T. Colonius and S. K. Lele, "Computational aeroacoustics: Progress on nonlinear problems of sound generation," Prog. Aerosp. Sci. **40**, 345 (2004).
[27]C. Bailly and C. Bogey, "Contributions of CAA to jet noise research and prediction," Int. J. Comput. Fluid Dyn. **18**, 481 (2004).
[28]M. Wang, J. B. Freund, and S. K. Lele, "Computational prediction of flow-generated sound," Annu. Rev. Fluid Mech. **38**, 483 (2006).
[29]J. B. Freund, "Noise sources in a low-Reynolds-number turbulent jet at Mach 0.9," J. Fluid Mech. **438**, 277 (2001).
[30]S. A. Stanley and S. Sarkar, "Influence of nozzle conditions and discrete forcing on turbulent planar jets," AIAA J. **38**, 1615 (2000).
[31]C. Bogey and C. Bailly, "Effects of inflow conditions and forcing on a Mach 0.9 jet and its radiated noise," AIAA J. **43**, 1000 (2005).
[32]F. Keiderling, L. Kleiser, and C. Bogey, "Numerical study of eigenmode forcing effects on jet flow development and noise generation mechanisms," Phys. Fluids **21**, 045106 (2009).
[33]J. Kim and H. Choi, "Large eddy simulation of a circular jet: Effect of inflow conditions on the near field," J. Fluid Mech. **620**, 383 (2009).
[34]C. Bogey and C. Bailly, "Influence of nozzle-exit boundary-layer conditions on the flow and acoustic fields of initially laminar jets," J. Fluid Mech. **663**, 507 (2010).
[35]C. Bogey, S. Barré, and C. Bailly, "Direct computation of the noise generated by subsonic jets originating from a straight pipe nozzle," Int. J. Aeroacoust. **7**, 1 (2008).
[36]A. Uzun and M. Hussaini, "Investigation of high frequency noise generation in the near-nozzle region of a jet using large eddy simulation," Theor. Comput. Fluid Dyn. **21**, 291 (2007).
[37]K. Mohseni and T. Colonius, "Numerical treatment of polar coordinate singularities," J. Comput. Phys. **157**, 787 (2000).
[38]C. Bogey and C. Bailly, "A family of low dispersive and low dissipative explicit schemes for flow and noise computations," J. Comput. Phys. **194**, 194 (2004).
[39]C. Bogey, N. de Cacqueray, and C. Bailly, "Finite differences for coarse azimuthal discretization and for reduction of effective resolution near origin of cylindrical flow equations," J. Comput. Phys. **230**, 1134 (2011).
[40]C. Bogey, N. de Cacqueray, and C. Bailly, "A shock-capturing methodology based on adaptative spatial filtering for high-order non-linear computations," J. Comput. Phys. **228**, 1447 (2009).
[41]J. Berland, C. Bogey, O. Marsden, and C. Bailly, "High-order, low dispersive and low dissipative explicit schemes for multiple-scale and boundary problems," J. Comput. Phys. **224**, 637 (2007).
[42]C. Bogey and C. Bailly, "Large eddy simulations of transitional round jets: Influence of the Reynolds number on flow development and energy dissipation," Phys. Fluids **18**, 065101 (2006).
[43]C. Bogey and C. Bailly, "Large eddy simulations of round free jets using explicit filtering with/without dynamic Smagorinsky model," Int. J. Heat Fluid Flow **27**, 603 (2006).
[44]C. Bogey and C. Bailly, "Turbulence and energy budget in a self-preserving round jet: Direct evaluation using large-eddy simulation," J. Fluid Mech. **627**, 129 (2009).
[45]C. K. W. Tam and Z. Dong, "Radiation and outflow boundary conditions for direct computation of acoustic and flow disturbances in a nonuniform mean flow," J. Comput. Acoust. **4**, 175 (1996).
[46]C. Bogey and C. Bailly, "Three-dimensional non reflective boundary conditions for acoustic simulations: Far-field formulation and validation test cases," Acta Acust. **88**, 463 (2002).
[47]C. Bogey, S. Barré, D. Juvé, and C. Bailly, "Simulation of a hot coaxial jet: Direct noise prediction and flow-acoustics correlations," Phys. Fluids **21**, 035105 (2009).
[48]K. K. Ahuja, B. J. Tester, and H. K. Tanna, "Calculation of far field jet noise spectra from near field measurements with true source location," J. Sound Vib. **116**, 415 (1987).
[49]V. Fleury, C. Bailly, E. Jondeau, M. Michard, and D. Juvé, "Space-time correlations in two subsonic jets using dual-PIV measurements," AIAA J. **46**, 2498 (2008).
[50]J. C. Lau, P. J. Morris, and M. J. Fisher, "Measurements in subsonic and supersonic free jets using a laser velocimeter," J. Fluid Mech. **93**, 1 (1979).
[51]H. K. Tanna, "An experimental study of jet noise. Part I: Turbulent mixing noise," J. Sound Vib. **50**, 405 (1977).
[52]C. Bogey, S. Barré, V. Fleury, C. Bailly, and D. Juvé, "Experimental study of the spectral properties of near-field and far-field jet noise," Int. J. Aeroacoust. **6**, 73 (2007).
[53]P. O. A. L. Davies, M. J. Fisher, and M. J. Barratt, "The characteristics of the turbulence in the mixing region of a round jet," J. Fluid Mech. **15**, 337 (1963).
[54]E. Mollo-Christensen, M. A. Kolpin, and J. R. Martucelli, "Experiments on jet flows and jet noise far-field spectra and directivity patterns," J. Fluid Mech. **18**, 285 (1964).
[55]P. A. Lush, "Measurements of subsonic jet noise and comparison with theory," J. Fluid Mech. **46**, 477 (1971).

[56]M. Schaffar, "Direct measurements of the correlation between axial in-jet velocity fluctuations and far field noise near the axis of a cold jet," J. Sound Vib. **64**, 73 (1979).
[57]J. Panda, R. G. Seasholtz, and K. A. Elam, "Investigation of noise sources in high-speed jets via correlation measurements," J. Fluid Mech. **537**, 349 (2005).
[58]C. Bogey and C. Bailly, "An analysis of the correlations between the turbulent flow and the sound pressure field of subsonic jets," J. Fluid Mech. **583**, 71 (2007).
[59]C. K. W. Tam, K. Viswanathan, K. K. Ahuja, and J. Panda, "The sources of jet noise: Experimental evidence," J. Fluid Mech. **615**, 253 (2008).
[60]S. B. Pope, *Turbulent Flows* (Cambridge University Press, Cambridge, UK, 2000).
[61]C. Bailly and G. Comte-Bellot, *Turbulence* (CNRS, Paris, 2003).